

The Summer Asia-North America Teleconnection and its Modulation by ENSO in Community Atmosphere Model, Version 5 (CAM5)

Kelsey Malloy (✉ kelsey.malloy@rsmas.miami.edu)

University of Miami Rosenstiel School of Marine and Atmospheric Science <https://orcid.org/0000-0002-1989-7490>

Ben P. Kirtman

University of Miami Rosenstiel School of Marine and Atmospheric Science

Research Article

Keywords: continental United States (CONUS), East Asian monsoon (EAM), Asia-North America (ANA), Community Atmospheric Model version 5 (CAM5), ENSO phases.

Posted Date: November 22nd, 2021

DOI: <https://doi.org/10.21203/rs.3.rs-1062059/v1>

License:  This work is licensed under a Creative Commons Attribution 4.0 International License.

[Read Full License](#)

Version of Record: A version of this preprint was published at Climate Dynamics on March 4th, 2022. See the published version at <https://doi.org/10.1007/s00382-022-06205-4>.

1 **The summer Asia-North America teleconnection and its modulation by ENSO in**
2 **Community Atmosphere Model, version 5 (CAM5)**
3
4
5
6
7
8
9

10
11
12
13 Kelsey Malloy¹, Ben P. Kirtman¹

14 ¹*Rosenstiel School of Marine and Atmospheric Science, University of Miami, Miami, Florida*
15
16
17
18
19
20
21
22
23

24 Corresponding author address:
25 Kelsey Malloy
26 kelsey.malloy@rsmas.miami.edu
27
28
29
30
31
32
33
34
35
36
37
38
39
40
41
42
43
44
45
46
47

Submit to *Climate Dynamics*

48
49
50
51
52
53
54
55
56
57
58
59
60
61
62
63
64
65
66
67

Abstract

Seasonal forecasts of summer continental United States (CONUS) rainfall have relatively low skill, partly due to a lack of consensus about its sources of predictability. The East Asian monsoon (EAM) can excite a cross-Pacific Rossby wave train, also known as the Asia-North America (ANA) teleconnection. In this study, we analyze the ANA teleconnection in observations and model simulations from the Community Atmospheric Model, version 5 (CAM5), comparing experiments with prescribed climatological SSTs and prescribed observed SSTs. Observations indicate a statistically significant relationship between a strong EAM and increased probability of positive precipitation anomalies over the U.S. west coast and the Plains-Midwest. The ANA teleconnection and CONUS rainfall patterns are improved in the CAM5 experiment with prescribed observed SSTs, suggesting that SST variability is necessary to simulate this teleconnection over CONUS. We find distinct ANA patterns between ENSO phases, with the La Niña-related patterns in CAM5_obsSST disagreeing with observations. Using linear steady-state quasi-geostrophic theory, we conclude that incorrect EAM forcing location greatly contributed to CAM5 biases, and jet stream disparities explained the ENSO-related biases. Finally, we compared EAM forcing experiments with different mean states using a simple dry nonlinear atmospheric general circulation model. Overall, the ANA pattern over CONUS and its modulation by ENSO forcing are well described by dry dynamics on seasonal-to-interannual timescales, including the constructive (destructive) interference between El Niño (La Niña) modulation and the ANA patterns over CONUS.

68 **1. Introduction**

69 The agricultural sector, water resource managers, and other preparedness agencies desire
70 monthly-to-seasonal rainfall forecasts for their decision-making, including for many vulnerable
71 regions of the continental United States (CONUS), such as the western U.S. and Great Plains.
72 However, there has been marginal success in providing reliable long-range forecasts of
73 precipitation in the warm season (Becker et al. 2014; Slater et al. 2016; Hao et al. 2018; Malloy
74 and Kirtman 2020), mostly due to relatively weak atmospheric flow as well as weaker signals
75 from El Niño-Southern Oscillation (ENSO) and the Madden-Julian Oscillation (MJO; Trenberth
76 et al. 1998; Zhou et al. 2012; Tian et al. 2017; Jha et al. 2019; Hu et al. 2020). For these reasons,
77 there is amplified interest within the scientific community to understand causes of CONUS
78 summer hydroclimate variability and its predictability.

79 Recent studies have indicated that quasi-stationary Rossby waves might be a key to
80 summertime predictability, especially for climate extremes (Liu et al. 1998; Ciancarelli et al.
81 2014; Lopez et al. 2019; DeAngelis et al. 2020; Lee et al. 2011; Schubert et al. 2011; Zhao et al.
82 2018; Beverley et al. 2019; Mariotti et al. 2020; Jong et al. 2021). Rossby waves can be excited
83 by remote sources, often guided by westerly jet streams as equivalent barotropic structures (Lau
84 and Weng 2002; Lee et al. 2009; Schubert et al. 2011; Moon et al. 2013; Zhu and Li 2016;
85 O'Reilly et al. 2018). These circumglobal patterns are a prominent mode of upper-level
86 circulation variability (Ding and Wang, 2005; Ding et al. 2011; Weaver et al. 2016); in fact, Lee
87 et al. (2011) estimated that up to 35% of the interannual variability in the mid-latitudes can be
88 attributed to near-circumglobal teleconnections. The causes of quasi-stationary Rossby wave
89 activity include distinct and joint influences from the Asian summer monsoon (ASM) and
90 ENSO, among other possible forcing.

91 The East Asian monsoon (EAM) is considered the northeastern branch of the ASM that
92 affects eastern China, Korea, and Japan (Ha et al. 2018). EAM precipitation and circulation is
93 typically out-of-phase with the western North Pacific monsoon (WNPM; Moon et al. 2013; Zhao
94 et al. 2015), another sub-system of the ASM located south of the EAM that affects southeast
95 Asia and the Philippines. Together, the EAM and WNPM comprise a northward-propagating rain
96 belt with variability on intraseasonal, seasonal, interannual, and interdecadal timescales (Wang et
97 al. 2001; Wang et al. 2008; Moon et al. 2013; Zhao et al. 2015; Lee and Wang 2016).

98 Because of its proximity to the East Asian jet, EAM heating is favorable for generating
99 Rossby wave responses (Lau and Weng 2002; Moon et al. 2013; Zhu and Li 2016; Zhao et al.
100 2018; Zhu and Li 2018). This upper-level wave pattern, the Asia-North America (ANA)
101 teleconnection, often traverses the North Pacific and reaches North America (Lau and Weng
102 2002; Zhu and Li 2016; Yang et al. 2020). Zhu and Li (2016) found that ANA is associated with
103 a northwest-southeast U.S. dipole of positive-negative rainfall anomalies. A series of AGCM
104 experiments in their study suggested that the EAM can force the ANA independent of ENSO.
105 There is a robust statistical and dynamical relationship between East Asian and North American
106 climate via this barotropic Rossby wave train (Wang et al. 2001; Moon et al. 2013; Zhao et al.
107 2018; Lopez et al. 2019; Yang et al. 2020), though influence is most evident in the Great Plains
108 and Midwest regions (Lopez et al. 2019).

109 The link between ENSO-forced North Pacific wave patterns and summer CONUS
110 hydroclimate is more complex. There is evidence that the warm phase of ENSO can excite the
111 Pacific-North America (PNA) teleconnection in the summer by itself (Schubert et al. 2002;
112 Pegion and Kumar 2010; Hu and Feng 2012; Zhu et al. 2013; Weaver et al. 2016), but results are
113 inconsistent. For example, Ciancarelli et al. (2014) showed that the influence of tropical Pacific

114 SST forcing is prominent in the early summer months, whereas Weaver et al. (2009) suggested
115 influence peaks in the late summer months.

116 Rather, the relationship between ENSO and CONUS hydroclimate may be more indirect;
117 ENSO affects EAM variability and/or the mean state in which EAM forcing responses
118 propagate. On the seasonal-to-interannual timescale, studies indicate that transitioning or
119 developing ENSO phases impact East Asian jet variability (Ting and Wang 1997; Du et al. 2016)
120 and/or EAM and WNPM precipitation variability (Wang et al. 2001; Wang et al. 2008; Wu et al.
121 2009; Zhao et al. 2015; Jong et al. 2021). Ding et al. (2011) found that ENSO can modulate the
122 strength of the EAM, altering North Pacific wave patterns. On the intraseasonal timescale, the
123 phase of ENSO can impact the period of the northward-propagating mode (Liu et al. 2016).
124 Finally, long-range predictability from EAM-related responses may come from ENSO (Lee et al.
125 2011; Liu et al. 2019; Zhou et al. 2020). Potential predictability of the EAM and its
126 teleconnections have been linked to interdecadal ENSO variability, i.e. there are decades when
127 ENSO has a greater influence on the EAM (Song and Zhou 2015; Zhu and Li 2018; Li et al.
128 2019).

129 There are several studies on the assessment of summer teleconnections and associated
130 North American hydroclimate in current global climate models, many of which demonstrate that
131 SST variability is vital for representing atmospheric circulation responses over CONUS (Weaver
132 et al. 2009; Hu and Feng 2012; Burgman and Jang 2015). Sheffield et al. (2013) found that
133 models in Coupled Model Intercomparison Project, version 5 (CMIP5) could not simulate
134 CONUS summer teleconnections and mechanisms related to its forced variability from SST
135 anomalies well. More specifically, North Pacific Rossby wave patterns related to a transitioning
136 Niño-to-Niña and western Pacific heating were weaker and inconsistent in Community

137 Atmosphere Model, version 5 (CAM5) without air-sea interaction (Jong et al. 2021). Air-sea
138 interaction improves EAM precipitation-SST connection (Liu et al. 2019; et al. Islam 2013;
139 Islam and Tang 2017), though there is realistic depiction of monsoonal precipitation climatology
140 and interannual variability in both CAM5 (Islam et al. 2013; Islam and Tang 2017) and CMIP5
141 (Sperber et al. 2013) overall.

142 Despite the perceived importance of Pacific SST variability, idealized atmospheric model
143 experiments with a prescribed summertime climatological background state from Zhu and Li
144 (2016) and Lopez et al. (2019) also produced the observed ANA pattern. In addition, there are
145 few studies that explicitly assess the ANA teleconnection in global climate models, including the
146 evaluation of predictability from prescribed SST variability. Therefore, our paper will address
147 the lack of understanding about the ANA teleconnection in observations as well as in a state-of-
148 the-art climate model. Using a simple framework, we isolated the EAM-forced and ENSO-
149 modulated circulation responses and precipitation impacts over CONUS. Due to emergent
150 literature on the important role of the mean or background state in climate models and skill in
151 teleconnection representation and prediction (Henderson et al. 2017; Kim et al. 2020; Wang et al.
152 2020), we diagnosed the roles of mean state and forcing in producing the ANA patterns and
153 related model biases on the long-range timescale.

154 Section 2 contains the description of the datasets, model experiments, and analysis
155 methods for the study. Results begin in Section 3, with the comparison of the ANA pattern
156 between observations and CAM5, including how ENSO influences this pattern. In Section 4, we
157 explain the circulation responses to EAM-related forcing and ENSO modulation as well as
158 model discrepancies using linear QG theory and additional simple dry AGCM experiments.

159 Finally, a summary and discussion of these results – including any complementary studies,
160 limitations, and suggested future work – are given in Section 5.

161 **2. Data and Methods**

162 *a. Observational datasets*

163 All observations are monthly values in the June-July-August (JJA) season for 1979-2019.
164 Zonal wind, meridional wind, geopotential height, temperature, and divergence data were
165 obtained from the European Centre for Medium-Range Weather Forecasts (ECMWF) fifth-
166 generation reanalysis (ERA5), which is provided on a 0.25° latitude/longitude grid (Hersbach et
167 al. 2020). Precipitation data were taken from Climate Prediction Center (CPC) Merged Analysis
168 of Precipitation (CMAP), which combines satellite and gauge data on a global 2.5°
169 latitude/longitude grid (Xie and Arkin 1997). Global SST data were taken from the Extended
170 Reconstructed Sea Surface Temperature, version 5 (ERSST-5), which is provided on a 2°
171 latitude/longitude grid (Huang et al. 2017).

172 *b. CAM5 experiments*

173 CAM5 is a global circulation model (GCM) and the atmospheric component of the
174 Community Earth System Model (CESM), developed by the National Center for Atmospheric
175 Research (NCAR; Neale et al., 2010). Atmosphere-only 30-year simulations were conducted
176 with prescribed global SSTs on an ocean data model. We analyzed monthly JJA output data with
177 a resolution of 0.47° latitude by 0.63° longitude and 30 vertical levels.

178 To investigate the role of SST variability on the ANA teleconnection, we performed two
179 experiments: one simulation with prescribed climatological SSTs (hereby referred to as
180 CAM5_climoSST), and the other simulation with prescribed observed SSTs (CAM5_obsSST).
181 The CAM5_obsSST experiment used the 1972-2001 period for SST data. This introduces global

182 SST variability (e.g. ENSO), compared to the CAM5_climoSST experiment, where the
183 prescribed time-mean SST data filters out this variability.

184 *d. Linear steady-state quasi-geostrophic solutions*

185 We explored the steady-state quasi-geostrophic (QG) linearity of the response to
186 prescribed divergence and mean state. This method starts with the linear QG vorticity equation:

$$187 \quad \frac{\partial \zeta_g}{\partial t} + v_g \cdot \nabla(\zeta_g + f) = -f_0 \nabla \cdot v \quad (1)$$

188 where ζ_g is the geostrophic vorticity, v_g is the geostrophic velocity, f is the Coriolis parameter,
189 f_0 is the Coriolis constant, and $\nabla \cdot v$ is the divergence. Focusing on the steady-state response,
190 using the mid-latitude beta-plane approximation ($f=f_0 + \beta v$), and viewing the divergence term
191 on the right-hand side as forcing (denoted as F), the equation becomes:

$$192 \quad u_g \frac{\partial \zeta_g}{\partial x} + \beta v_g = F \quad (2)$$

193 The first term on the left-hand side is the advection of geostrophic relative vorticity by the
194 geostrophic zonal wind, and the second term on the left-hand side is the advection of planetary
195 vorticity by the geostrophic meridional wind. These terms “compete” to balance the divergence
196 forcing term on the right-hand side. Finally, we linearize the equation about a prescribed time
197 mean geostrophic zonal wind and solve for the geostrophic meridional wind via a fixed-point
198 iteration. The calculated meridional wind field is converted to a geopotential height field.

199 In using this equation, we are interested in how differences in the mean state, $\overline{u_g}$ (hereby
200 referred to as \overline{U}) and EAM-related divergence forcing, F , alter the linear QG response, which is
201 the ANA pattern in this study. We specified \overline{U} as the 250-hPa zonal wind (U250) climatology
202 and the divergence forcing (F) as the strong – weak EAM 250-hPa divergence (DIV250)

203 anomaly composite. These values are taken from observations, CAM5_climoSST, or
204 CAM5_obsSST. We also considered \bar{U} and F that are conditioned on ENSO state (Niño or Niña)
205 to assess the importance of indirect ENSO modulation of responses and biases. Finally, we tested
206 direct ENSO modulation by adding tropical Pacific El Niño or La Niña divergence forcing and
207 subtracting that response from response with only EAM forcing.

208 *c. Dry AGCM experiments*

209 To isolate the dry atmospheric processes, we also tested EAM forcing with a dry,
210 baroclinic, nonlinear AGCM. This is a spectral model with Rhomboidal truncation at R42, which
211 equates to a 1.7° latitude by 2.8° longitude grid, and it has 26 vertical levels. The model solves
212 the full primitive equations of divergence, vorticity, temperature and surface pressure. The
213 AGCM is adapted from Brenner et al. (1984) to remove moist processes. Newtonian cooling is
214 specified throughout the troposphere with enhanced damping near the surface. Rayleigh friction
215 is specified at the lower levels and mimic realistic land-sea frictional contrasts. Versions of this
216 dry AGCM have been used in Kirtman et al. (2001) and is described in detail in Brenner et al.
217 (1984). This simple, idealized model is used for evaluating the large-scale teleconnections,
218 primarily quasi-stationary wave activity and dry dynamic processes.

219 The model requires a mean state as input, with an option to add heating forcing. The JJA
220 surface temperature climatology is input as mean state for the model. Climatology was calculated
221 from ERA5, CAM5_climoSST, and CAM5_obsSST data and interpolated to the model's grid.
222 Each experiment with the respective mean state was integrated forward for 900 days, but
223 analysis excluded the spin-up period of 100 days. EAM-forced responses are calculated by
224 performing an experiment with EAM heating and then performing an experiment without EAM
225 heating, both in the same mean state, and subtracting the difference. The EAM-forced

226 experiments apply a constant diabatic heating via Gaussian bubble with a maximum of 2 K day^{-1}
227 centered at 30°N , 120°E and 300 hPa (see Supp. Fig. 1), similar to Zhu and Li (2016). Note that
228 we also tested strong – weak EAM by running an experiment with positive heating forcing and
229 an experiment with negative heating (cooling) in EAM location. Because patterns were similar,
230 they have been excluded for the sake of brevity.

231 Finally, we address both indirect and direct ENSO modulation to the EAM-forced
232 response as we did with the linear QG solutions: Indirect ENSO modulation was assessed by
233 adjusting the observed and CAM5_obsSST mean state based on surface temperature climatology
234 composited during El Niño or La Niña months, and direct ENSO modulation was assessed by
235 running experiments with both ENSO-related forcing and EAM forcing and subtracting that
236 response by the original EAM-forced response. El Niño heating/La Niña cooling forcing location
237 was chosen based on El Niño – La Niña divergence anomaly composites. A list and description
238 of the experiments and their differences in purpose and setup can be found in Table 1.

239 *e. EAM and ENSO definitions*

240 The EAM index was defined by upper-level circulation as in Zhao et al. (2015):
241 $\text{Std}[U_{200}(2.5-10^\circ\text{N}, 105-140^\circ\text{E}) - U_{200}(17.5-22.5^\circ\text{N}, 105-140^\circ\text{E}) + U_{200}(30-37.5^\circ\text{N}, 105-$
242 $140^\circ\text{E})]$, where U_{200} is the 200-hPa zonal wind averaged within the domain outlined in the
243 parentheses, and Std indicates a standardization of the timeseries of the index. Strong and weak
244 EAM events are determined by the upper and lower terciles of the index, respectively. We chose
245 this index because it characterizes the distinct EAM and WNPM precipitation anomalies,
246 captures multiple timescales of variability, and has been linked to ENSO (Zhao et al. 2015).

247 We categorized ENSO events using the Niño3.4, defined as $[T^*(5^\circ\text{S}-5^\circ\text{N}, 170-120^\circ\text{W})]$,
248 where T^* denotes SST anomalies. Niño events were defined by a monthly Niño3.4 index greater

249 or equal to 0.5°C , and Niña events were defined by a monthly Niño3.4 index less than or equal to
250 0.5°C . Otherwise, the ENSO event was considered neutral.

251 **3. The ANA Teleconnection in Observations and CAM5**

252 *a. EAM-related precipitation and circulation patterns*

253 The ANA teleconnection is the bridge between EAM rainfall and CONUS rainfall. First,
254 we established this relationship using difference composites, calculated by subtracting the
255 averaged precipitation anomalies during strong EAM events by the averaged precipitation
256 anomalies during weak EAM events and standardizing the difference. The strong – weak EAM
257 precipitation standardized anomalies are seen in Fig. 1 (left column). In observations (top left),
258 the EAM structure is established, with significant positive rainfall anomalies within the $25\text{-}35^{\circ}\text{N}$
259 latitudinal belt and stretched over the western and central North Pacific. Negative rainfall
260 anomalies are located south and north of the EAM rainfall belt as a part of the full monsoonal
261 circulation. Over CONUS, there are two regions that have statistically significant EAM-related
262 precipitation anomalies: the west coast and Plains-Midwest regions (corresponding purple and
263 magenta boxes). To analyze further, we found the kernel density estimation (KDE) of the
264 standardized precipitation anomalies at each month and grid point within the box for the strong
265 EAM events and weak EAM events (right columns). The distribution of strong EAM anomalies
266 (red) is shifted right from the weak EAM anomalies (blue), indicating that a strong EAM is
267 associated with a higher probability of wet anomalies in these regions. The CONUS difference
268 composite pattern, though not statistically significant everywhere, is analogous to the northwest-
269 southeast rainfall dipole from Zhu and Li (2016).

270 Generally, the CAM5_climoSST standardized precipitation anomaly difference
271 composite (Fig. 1, middle left) is similar to the observed over the EAM region. Over CONUS,

272 the associated precipitation anomalies over the west coast are positive, but anomalies over the
273 Plains-Midwest are negative, unlike observations. The KDEs (middle right) corroborate this
274 result: there is a higher probability of wet anomalies during a strong EAM over the west coast,
275 most apparent at the right tail, and there is decreased probability of wet anomalies over the
276 Plains-Midwest during strong EAM events.

277 The precipitation anomaly pattern is more comparable to the observations in the
278 CAM5_obsSST standardized precipitation difference composite (Fig. 1, bottom left). The
279 structure of the anomalies for the entire monsoonal system is better represented. The CONUS
280 precipitation anomaly pattern is improved, particularly over the Plains-Midwest, though these
281 wet anomalies also extend to the southern Plains. However, there are dry anomalies in the
282 eastern North Pacific and southern west coast that are not present in observations. The KDEs for
283 the west coast indicate a minor shift in the distribution of precipitation anomalies to the right.
284 However, there is not a clear distribution shift over the Plains-Midwest. This may suggest that
285 the EAM-CONUS rainfall relationship is more affected by local processes in the model. Overall,
286 CAM5_obsSST is able to capture the rainfall pattern, and we attempt to address biases or
287 discrepancies in the remainder of the study by interpreting Rossby wave responses.

288 On this timescale of interest, the anomalous zonally-asymmetric component of the
289 circulation, stationary eddies, controls the pattern of anomalous moisture transport and rainfall
290 (Liu et al. 1998). Fig. 2 shows the zonally-asymmetric component of the strong – weak EAM
291 Z250 anomaly difference composite ($\overline{Z250}^*$). In observations (top), a strong EAM is associated
292 with a wave train pattern oriented meridionally over East Asia and Siberia. An anomalous ridge
293 stretches from the EAM region to the North American coast, an anomalous trough is found off
294 the coast of Baja California/U.S. southwest and across the Gulf of Mexico, and an anomalous

295 ridge is centered over Quebec/Hudson Bay. This pattern is weak over North America, but it is
296 generally in agreement with previous studies that showed that anomalous troughs over western
297 U.S. are important to identify southerly winds and moisture transport into CONUS, fueling
298 precipitation events (Mallakpour and Villarini 2016; Malloy and Kirtman 2020).

299 Unlike observations, the $\overline{Z250}^*$ difference composite pattern from CAM5_climoSST has
300 more of a zonal wave train structure from the EAM region to North America, and, over North
301 America, the west-east pattern is opposite to observations. The $\overline{Z250}^*$ difference composite
302 pattern from CAM5_obsSST has a noticeably improved representation of the teleconnection over
303 North America. This also dynamically explains the better comparison of the standardized
304 precipitation anomaly differences between observations and CAM5_obsSST from Fig. 1. In
305 general, including prescribed global SST variability in CAM5 improved the representation of the
306 ANA pattern and its associated precipitation patterns over North America. Even in the EAM
307 region, the local stationary wave pattern in the observations is not particularly well captured by
308 the model, somewhat surprisingly, although arguably better with observed SST forcing.

309 *b. EAM-related patterns separated by ENSO phase*

310 On seasonal-to-interannual scales, ENSO has been found to have an influence on the
311 EAM response (Ding et al. 2011); therefore, conditioning the EAM-related pattern on ENSO
312 phases for observations and CAM5_obsSST may reveal different impacts downstream.

313 The observed conditioned strong – weak EAM composites of standardized precipitation
314 anomalies and $\overline{Z250}^*$ validate that ENSO phase is important for understanding CONUS
315 impacts. Fig. 3 shows the classification of the difference composites from Fig. 1 and 2 into
316 ENSO phases by finding the strong – weak EAM during El Niño (top row), neutral ENSO
317 (middle row), and La Niña (bottom row) months. Over the Plains-Midwest, EAM-related

318 precipitation anomalies (left column) during El Niño are more robust than during neutral ENSO
319 or La Niña. The west coast anomalies are less sensitive to ENSO phase, showing statistically
320 significant wet anomalies during the neutral phase. The largest differences in $\overline{Z250}^*$ are over the
321 eastern North Pacific and North America (right column), with La Niña being associated with an
322 anomalous ridge over most of Canada and the Pacific Northwest. By examining the KDEs
323 (middle columns) of the standardized precipitation anomalies, during La Niña, the Plains-
324 Midwest has a greater probability of dry anomalies during a strong EAM.

325 The weaknesses in the model capturing the observed EAM-CONUS teleconnections are
326 amplified when stratifying by ENSO phase. As seen in Fig. 4, there are wet anomalies over the
327 west coast and Plains-Midwest during neutral ENSO months (left middle), further established by
328 the slight shift in distribution for strong EAM events. The west coast precipitation anomalies are
329 contingent on ENSO phase in CAM5_obsSST: during El Niño (top left), there is a north-south
330 pattern of wet-dry anomalies and no discernible difference in the KDEs (top right) between
331 strong and weak EAM months, and, during La Niña (bottom left), there is a greater probability of
332 wet anomalies overall. The $\overline{Z250}^*$ patterns over North America are also dissimilar: during El
333 Niño, the $\overline{Z250}^*$ difference composite is not statistically significant over North America (top
334 right), and, during La Niña, there is a cross-Pacific wave train response, with an anomalous
335 trough over western North America and an anomalous ridge over eastern North America (bottom
336 right). This explains the extreme positive precipitation anomalies in the composites (bottom left)
337 and increased probability of positive precipitation anomalies over the Plains-Midwest seen in the
338 KDE shifts. Overall, the ENSO-modulated ANA teleconnection is not well represented in
339 CAM5_obsSST, especially during La Niña.

340 We note that one limitation of this experimental design is that the observations and model
341 include different time periods: 1979-2019 for observations and 1972-2001 for CAM5_obsSST.
342 However, we performed the same analysis for the overlap period – 1979-2001 – and found that
343 results overall were similar and only subtle differences exist (cf. Supp. Figs. 2 and 3). Therefore,
344 the different time periods between model and observations does not explain the discrepancies.

345 The ANA teleconnection was better represented in CAM5_obsSST, the experiment that
346 simulated global SST variability. Yet, the distinct patterns from the ENSO phases were unlike –
347 even opposite to – the observations. This motivates a need to understand the EAM-forced and
348 ENSO-influenced responses. What are the roles of the mean state and divergence forcing, and
349 why does the model fail to capture the observed relationships?

350 **4. The Roles of Mean State and Forcing**

351 *a. Steady-state linear QG solution results*

352 The linear QG analysis presented here is examining the extent to which the EAM-
353 CONUS ANA teleconnection can be understood in this simple framework. Essentially, the extent
354 to which the linear QG model captures the CONUS component of the teleconnection can be used
355 to understand, at least in part, why CAM5 fails and further bolsters the simple interpretation of
356 the observational results.

357 As described in Section 2, the steady-state linear QG solution to EAM forcing in the mid-
358 latitudes depends on the divergence forcing (F) structure and a mean state (\bar{U}), both of which are
359 different between the observations, CAM5_climoSST experiment, and CAM5_obsSST
360 experiment. Fig. 5 summarizes the different linear QG Z250 responses and attempts to isolate the
361 \bar{U} and F “contribution” to the pattern. The observed response can be seen in the top panel: when
362 inputting U250 climatology as \bar{U} and strong – weak EAM DIV250 anomaly composite over

363 EAM region as F, the solution is a meridionally oriented Z250 pattern over the EAM region and
364 a zonally oriented wave train over the North Pacific and North America. While not perfect, there
365 are many similarities to the ANA pattern from Fig. 2 (top), particularly the response over the
366 EAM region and generally over the eastern North Pacific and North America.

367 The CAM5_climoSST response (Fig. 5, left middle) – obtained by inputting its separate
368 U250 climatology and DIV250 anomaly composite – is much different. The mid-latitude
369 response matches the overall pattern from Fig. 2 (middle); the ANA teleconnection from
370 CAM5_climoSST can be described by the steady-state linear QG response the EAM forcing.
371 Interestingly, the CAM5_obsSST response (left bottom) looks identical to the CAM5_climoSST
372 response despite the stark differences over CONUS seen in Fig. 2.

373 We next fixed F as the divergence anomalies from observations (Fig. 5, middle column),
374 keeping \bar{U} as corresponding to CAM5_climoSST or CAM5_obsSST, which improves the ANA
375 pattern overall. The response over the EAM region improves, and the response with the \bar{U} from
376 CAM5_obsSST (middle bottom) looks more like its EAM-related pattern from Fig. 2 (bottom),
377 especially over the mid-latitude Pacific, Alaska, and southwest U.S. This suggests that F greatly
378 influences the structure of the ANA pattern, and the F biases in CAM5 are limiting its
379 representation of the pattern. In addition, the contrasts in the Z250 response via \bar{U} differences
380 between CAM5_climoSST and CAM5_obsSST are highlighted. Though subtle, the different \bar{U}
381 (jet stream climatologies) in these CAM5 experiment can perhaps explain some aspect of the
382 different Z250 responses over the North Pacific.

383 We also fixed \bar{U} as the U250 climatology from observations (Fig. 5, right column) and
384 kept F as corresponding to CAM5_climoSST or CAM5_obsSST, confirming former findings.
385 The structure of these responses looks similar to the CAM5 responses without the fixed \bar{U} (left

386 middle and left bottom), and dissimilar to the observed response (top), further validating the
387 importance of improving the EAM-related divergence forcing, F , to correct the ANA pattern and
388 associated impacts over CONUS.

389 In brief, the linear QG solutions captured many aspects of the observed ANA
390 teleconnection (cf. Fig. 5 vs. Fig. 2). The misrepresentation of the ANA teleconnection in CAM5
391 is greatly influenced by the CAM5 biases in the EAM forcing (F). Differences between the two
392 CAM5 simulations (CAM5_climoSST vs. CAM5_obsSST) are very subtle and not well
393 explained by this linear QG framework.

394 To understand the indirect ENSO influence on the ANA pattern in observations and the
395 CAM5_obsSST simulation, F was conditioned on ENSO phase before solving for the Z250
396 response, i.e. F was input as the strong – weak EAM DIV250 anomaly during El Niño or La
397 Niña. In Fig. 6, for the observed Z250 EAM-forced responses (left column) during El Niño (top)
398 and La Niña (bottom), there is little difference. This is also true for the CAM5_obsSST
399 responses (right column). ENSO's influence on the location/structure of EAM divergence
400 forcing does not modulate the ANA pattern. Nevertheless, the disparities between the observed
401 (left column) and CAM5_obsSST (right column) responses can still be described by the
402 differences in the F location/structure, once again.

403 \bar{U} was also conditioned on ENSO phase, i.e. \bar{U} was taken as the U250 composite during
404 El Niño or La Niña, and stark differences between the responses with El Niño-related \bar{U} and La
405 Niña-related \bar{U} are discerned in Fig. 7. In observations, the Z250 response with El Niño-related
406 \bar{U} (top left) is more amplified and has an eastward-shifted structure. Interestingly, the canonical
407 El Niño pattern (typically linked to winter) is observed over North America, with an anomalous
408 trough over southern CONUS and an anomalous ridge north of it. In contrast, the response with

409 the La Niña-related \bar{U} (bottom left) has an opposite pattern, closer to the response not
410 conditioned on ENSO in Fig. 5 (top).

411 The CAM5_obsSST solutions reveal the limitations of the model mean state during
412 ENSO. The response with the El Niño-related \bar{U} (Fig. 7, top right), like the observed response,
413 has a wave pattern over the North Pacific, with an anomalous trough over the eastern North
414 Pacific and anomalous ridge over the high-latitudes of North America. The wavelength of this
415 pattern is shorter with the \bar{U} from CAM5_obsSST, and it does not include the anomalous trough
416 over southern CONUS, but there are many parallels. Conversely, the response with the La Niña-
417 related \bar{U} has very little resemblance to the La Niña-related response from observations.

418 In short, conditioning the \bar{U} on ENSO does seem to explain (1) the variability in the ANA
419 pattern and (2) large model biases in CAM5_obsSST during La Niña months. However, we note
420 that these responses are not comparable to Figs. 3 and 4 (top, bottom), particularly over CONUS.

421 Direct ENSO modulation is most apparent over CONUS, seen in Fig. 8. In observations,
422 El Niño modulation (top left) leads to an amplification of the EAM-forced response over
423 CONUS (cf. Fig 5, top left) and La Niña modulation (bottom left) leads to a weakening.
424 Although the ENSO forcing in the tropical Pacific is much stronger in CAM5_obsSST than
425 observations (purple and green contours), the CAM5_obsSST solutions for El Niño modulation
426 (top right) and La Niña modulation (bottom right) are weaker. There is little difference between
427 ENSO phases over CONUS, suggesting that CAM5_obsSST ENSO-related mean state
428 differences are not substantial enough to impact indirect ENSO modulation in CAM5.

429 Despite the usefulness in the linear QG solutions and framework, there are aspects of the
430 ANA teleconnection, such as the subtropical Pacific response, not captured. In addition, this
431 framework does not address concerns about variability of this response; differences in mean state

432 between observations and CAM5 may influence the robustness of the EAM-forced response.
433 Finally, while we added direct ENSO-related divergence forcing to this model to assess direct
434 modulation, it is possible that their interaction is nonlinear. For these reasons, we utilize the dry
435 nonlinear AGCM.

436 *b. Dry nonlinear AGCM experiment results*

437 The dry, nonlinear AGCM can test the sensitivity of responses with different mean states
438 while also determining the robustness of the EAM-forced circulation response. Robustness is
439 measured by calculating the 90-day moving mean standard deviation (σ) of the response, and
440 dividing the responses according to this moving mean standard deviation σ . The following
441 results are from experiments where the heating forcing location was based on the observed
442 EAM-related divergence anomalies (Fig. 5, top left). Results for the EAM-forced experiments
443 with the mean states from CAM5 when the heating forcing is 10° eastward shift (based on Fig. 5,
444 middle and bottom left) are provided in Supp. Fig. 4, though the findings are similar.

445 In Fig. 9, when the observational climatology was input as the mean state (top row), the
446 $\overline{Z250}^*$ response (left column) includes a robust elongated anomalous ridge over the North
447 Pacific and anomalous trough centered over the southwestern U.S., indicated by the $>+1\sigma$ and $<-$
448 1σ anomalies, respectively. By comparing to Fig. 2 (top), it is apparent that the dry atmospheric
449 dynamics in this AGCM can effectively simulate the observed ANA teleconnection. Because this
450 is a dry model, we can consider the time-mean DIV250 response (right column) as a proxy for
451 large-scale precipitation patterns associated with the heating forcing. The observed DIV250
452 response also corresponds with EAM-related patterns from Fig. 1 (top left). There is upper-level
453 divergence over the western coast, central U.S., and regions of Quebec, which are dynamically
454 linked to the wet anomalies. Additionally, there is upper-level convergence over

455 Alberta/Northwest Territories, southwest U.S., and the eastern coast, dynamically linked to dry
456 anomalies. However, this response is relatively weak as σ values are low; this suggests that
457 large-scale precipitation patterns due to EAM heating forcing are subject to significant variability
458 on the seasonal-to-interannual timescales. In fact, differences/modulation of DIV250 responses
459 are not discernible and not robust (Figs. 10-13, right column); therefore, we concentrate on
460 $\overline{Z250}^*$ responses/differences for remainder of results.

461 Over East Asia and North Pacific, the dry AGCM responses when the CAM5_climoSST
462 and CAM5_obsSST experiment climatologies were input as the mean state are well represented
463 (Fig. 9, middle and bottom row). The $\overline{Z250}^*$ response is a more zonal wave pattern,
464 corresponding well to Fig. 2 (middle and bottom). However, the strong anomalous trough
465 centered over southern U.S. and northern Mexico in the dry AGCM is unlike the composite
466 pattern in Fig. 2. The DIV250 responses are not significantly different from the experiment with
467 the mean state from observations. Overall, while the dry AGCM responses can explain CAM5
468 ANA patterns over the North Pacific well, there are discrepancies over North America between
469 the dry AGCM responses and composite patterns that suggest additional processes are likely to
470 be important. Other sources of forcing (e.g. ENSO) and/or land-atmosphere feedbacks may
471 significantly contribute in simulating the ANA teleconnection in CAM5 experiments.

472 The dry AGCM response differences in Figs. 10 and 11 suggest that El Niño- or La Niña-
473 related mean state differences alter the responses, confirming the steady-state linear QG solution
474 results. The difference in dry AGCM $\overline{Z250}^*$ response with the observational El Niño-composited
475 climatology as the mean state (Fig. 10, top left) has an anomalous ridge over high-latitude East
476 Asia, an anomalous trough centered over the Bering Sea, an anomalous ridge over the Gulf of
477 Alaska, and an anomalous trough over central North America. This is opposed to the response

478 with the La Niña-composited climatology as the mean state (Fig. 11, top left), which reveals an
479 opposite pattern. By comparing with the conditional composites from Figs. 3 (right column), we
480 find that the indirect modulation with the dry AGCM simulates ENSO-related patterns overall
481 over North America, but not over East Asia and the North Pacific.

482 The responses with the CAM5_obsSST Niño- and Niña-composited climatologies (Figs.
483 10 and 11, bottom left) are very similar to each other, just as with the linear QG solutions.
484 ENSO-related mean state differences are not strong in CAM5, reducing indirect ENSO
485 modulation. By comparing with the conditional composites from Fig. 4 (right column), we
486 observe that the dry AGCM does not capture the ENSO-related patterns from CAM5 well
487 overall, but there is somewhat more of a zonally oriented trough-ridge pattern over CONUS
488 associated with the response with the La Niña-composited climatology, as in Fig. 4 (bottom
489 right). In general, indirect ENSO modulation may not be sufficient in describing the ENSO-
490 related ANA patterns in this dry AGCM, especially over the North Pacific and for patterns from
491 CAM5_obsSST.

492 We effectively extract direct ENSO modulation, seen in Figs. 12 and 13. Note that these
493 should be interpreted as only the ENSO-modulated portion of the response, not the total EAM-
494 and ENSO-forced response. The El Niño-modulated $\overline{Z250^*}$ with the observational mean state
495 (Fig. 12, top left) shows a band of negative anomalies stretched over the subtropical Pacific,
496 which would weaken the EAM-forced elongated North Pacific ridge and strengthen the trough
497 over western CONUS (cf. Fig 9, top). In addition, there are positive anomalies over Alaska and
498 central-eastern CONUS. Collectively, this results suggests that El Niño promotes strengthening
499 of the west-east trough-ridge pattern, or constructive interference with the ANA pattern, over
500 CONUS, influencing enhanced precipitation over the Plains-Midwest (cf. Figs. 3, top left).

501 Conversely, the La Niña-modulated $\overline{Z250}^*$ with the observational mean state (Fig. 13, top left)
502 shows positive anomalies in the subtropical Pacific and western CONUS. The pattern over North
503 America is opposite to El Niño-modulated $\overline{Z250}^*$, suggesting destructive interference with the
504 EAM-forced trough over western CONUS and explaining the decreased precipitation over the
505 Plains-Midwest during La Niña.

506 El Niño- and La Niña-modulated $\overline{Z250}^*$ with the CAM5_obsSST mean state (Figs. 12
507 and 13, bottom left) have similar destructive and constructive interference of ANA pattern,
508 respectively, over the subtropical Pacific, as in the results with the observational mean state.
509 However, there is an anomalous ridge centered over CONUS in both the El Niño- and La Niña-
510 modulated $\overline{Z250}^*$ patterns, not aligning with observations nor explaining the ENSO-related
511 patterns from Fig. 4. Again, CONUS patterns in the dry AGCM with the CAM5_obsSST mean
512 state are not simulated well, perhaps emphasizing the differences in the important processes
513 behind the ANA pattern in observations and CAM5.

514 **4. Summary and Discussion**

515 Summer CONUS rainfall remains a forecast challenge. Understanding rainfall variability
516 and its links with quasi-persistent features, e.g. monsoons and SST anomalies, is imperative for
517 long-range forecasting. In this study, we established the statistical and dynamical relationship
518 between the EAM and CONUS precipitation and circulation anomaly patterns, the ANA
519 teleconnection, which impacts the U.S. west coast and Plains-Midwest regions (Figs. 1 and 2).
520 This confirmed Zhu and Li (2016) study's ANA rainfall pattern and the many studies that have
521 linked Plains-Midwest climate to EAM activity (Lopez et al. 2019), but the link between the
522 EAM and U.S. west coast precipitation is relatively novel. We compared the ANA pattern from
523 observations to its representation in a state-of-the-art atmospheric model, CAM5, where one

524 experiment prescribed global climatological SSTs (CAM5_climoSST), and the other prescribed
525 global observed SSTs (CAM5_obsSST). The ANA patterns from the CAM5_obsSST experiment
526 were more similar to observations, suggesting that SST variability is important for simulating
527 this teleconnection, although some notable difference between CAM5_obsSST and the
528 observations were identified.

529 Because ENSO has an established influence on the EAM (Wang et al. 2001; Wang et al.
530 2008; Ding et al. 2011), we investigated the effect of ENSO's modulation on the ANA
531 teleconnection in observations and CAM5_obsSST (Figs. 3 and 4). The ANA patterns did
532 depend on ENSO phase over the Plains-Midwest region. However, representation of the ENSO-
533 modulated ANA patterns in CAM5_obsSST was limited; in fact, Niña-related ANA patterns
534 over the Plains-Midwest between observations and CAM5_obsSST were of opposite sign (dry
535 vs. wet anomalies, respectively).

536 Next, we used steady-state linear QG solution framework and a dry nonlinear AGCM to
537 diagnose to what extent the observations and the CAM5 simulations can be understood in terms
538 in this simplified framework as well as how much of the ANA teleconnection is due to nonlinear
539 processes. We summarize the results from this section as follows:

- 540 1. CAM5 limitations in representing the ANA pattern are due to CAM5 biases in the EAM
541 forcing location/structure (Figs. 5-8).
- 542 2. Conditioning the mean state on ENSO generates distinctive ANA patterns. The biases in
543 the ENSO-related mean state in CAM5_obsSST at least partly describes the erroneous
544 representation of the La Niña-related ANA teleconnection in CAM5_obsSST (Fig. 7).
- 545 3. Nonlinear, dry atmospheric dynamics is essential for producing the EAM-forced pattern
546 (cf. Fig 9, top and Fig. 2, top), particularly over the subtropics.

547 4. Both indirect ENSO modulation and direct ENSO modulation are important for
548 simulating details of the ANA pattern over CONUS (Figs. 8, 12 and 13). Generally,
549 constructive (destructive) interference of El Niño (La Niña) patterns with the ANA
550 pattern over CONUS explains enhanced (weakened) precipitation signals, particularly
551 over the Plains-Midwest, which is reproduced well in both the linear QG solutions and
552 nonlinear dry AGCM.

553 These results complement previous studies that explored teleconnection sensitivity to mean
554 state (Henderson et al. 2017; Kim et al. 2020; Wang et al. 2020); model mean state, especially
555 relating to jet stream strength and location, is essential for simulating correct Rossby wave
556 responses and downstream impacts (O'Reilly et al. 2018).

557 Not all features of the ANA pattern nor the CAM5 biases were simulated/explained
558 sufficiently with the linear QG model nor the dry AGCM (e.g. discrepancies over CONUS
559 patterns between the dry AGCM responses with CAM5 mean states cf. Figs. 9-13 and CAM5
560 ANA pattern over CONUS in Figs. 2 and 4). Neither model has land-moisture feedbacks, which
561 are likely key in simulating the combined EAM and ENSO influence. Generally, summertime
562 predictability has been linked to soil moisture and atmosphere-land processes (Dirmeyer et al.
563 2003; Koster et al. 2006; Schubert et al. 2008; Burgman and Jang 2015; Jong et al. 2021);
564 therefore, there should be more analysis done on specific connections between ANA-related
565 rainfall and atmosphere-land coupling.

566 Future studies should consider additional sources of SST variability besides ENSO.
567 Previous studies have suggested that North Atlantic SST variability is vital for understanding
568 CONUS hydroclimate (Schubert et al. 2008; Weaver et al. 2009; Malloy and Kirtman 2020).
569 Extratropical Pacific SST variability (e.g. Pacific Decadal Oscillation) influences both ENSO

570 events and mid-latitude Rossby wave propagation on the interdecadal timescale (Lee et al. 2011;
571 Zhu et al. 2013; Burgman and Jang 2015; Song and Zhao 2015). Indian Ocean SST variability,
572 including the Indian Ocean Dipole (IOD), interacts with both ENSO and ASM variability (Islam
573 et al. 2013; Du et al. 2016; Lee and Wang 2016).

574 The study's focus was on contemporary, monthly-mean ENSO modulation of the ANA
575 teleconnection, but the transitional, slowly evolving aspects of ENSO-EAM links (e.g. post-peak
576 Niño effects) might also be important (Weaver et al. 2016; Li et al. 2019). ENSO variability on
577 the interdecadal timescale (Wu et al. 2009; Zhu and Li 2018) may change how it modulates the
578 ANA pattern or robustness/predictability of responses.

579 Both complex AGCMs and simple dry AGCMs were employed to isolate processes
580 needed to reproduce the ANA teleconnection, ENSO modulation, and their impact on CONUS
581 circulation and rainfall. Whether or not the better understanding of the predictability of quasi-
582 persistent teleconnections and Rossby wave responses translates to an increase in long-range
583 rainfall forecast skill remains an open question.

584

585

Acknowledgements

586 The authors acknowledge the National Center for Atmospheric Research for access to the
587 Community Earth System Model to conduct the prescribed SST experiments. We also thank the
588 University of Miami Institute for Data Science and Computing (IDSC) for computational
589 resources to complete the dry nonlinear AGCM model experiments. This work was supported
590 through NOAA Grants NA15OAR4320064, NA16OAR4310141, N16OAR4310149 and
591 NA20OAR430472 and DOE Grant DE-SC0019433. The authors have no competing interests to
592 declare relevant to the content of this article.

593

594

Data Availability Statement

595

All data analyzed in this study are described in this article, including relevant citations for

596

accessing the data. Model data are available upon reasonable request.

597

- 599 Becker, E., H.v. den Dool, and Q. Zhang. (2014). Predictability and Forecast Skill in NMME. *J.*
600 *Climate*, 27, 5891–5906, <https://doi.org/10.1175/JCLI-D-13-00597.1>.
- 601 Beverley, J. D., Woolnough, S. J., Baker, L. H., Johnson, S. J., & Weisheimer, A. (2019). The
602 northern hemisphere circumglobal teleconnection in a seasonal forecast model and its
603 relationship to European summer forecast skill. *Climate dynamics*, 52(5), 3759-3771,
604 <https://doi.org/10.1007/s00382-018-4371-4>.
- 605 Brenner, S., Mitchell, K. (Kenneth Erwin)., Yang, C., U.S. Air Force Geophysics Laboratory.
606 Atmospheric Sciences Division. (1984). The AFGL global spectral model: expanded resolution
607 baseline version. Hanscom AFB, Massachusetts: Air Force Geophysics Laboratory, Air Force
608 Systems Command, United States Air Force. (Retrieved from
609 <https://catalog.hathitrust.org/Record/102326036/Home>)
- 610 Burgman, R. J., and Y. Jang. (2015). Simulated U.S. Drought Response to Interannual and
611 Decadal Pacific SST Variability. *J. Climate*, 28, 4688–4705, [https://doi.org/10.1175/JCLI-D-14-](https://doi.org/10.1175/JCLI-D-14-00247.1)
612 [00247.1](https://doi.org/10.1175/JCLI-D-14-00247.1).
- 613 Ciancarelli, B., Castro, C. L., Woodhouse, C., Dominguez, F., Chang, H. I., Carrillo, C., &
614 Griffin, D. (2014). Dominant patterns of US warm season precipitation variability in a fine
615 resolution observational record, with focus on the southwest. *International journal of*
616 *climatology*, 34(3), 687-707, <https://doi.org/10.1002/joc.3716>.
- 617 DeAngelis, A. M., Wang, H., Koster, R. D., Schubert, S. D., Chang, Y., & Marshak, J. (2020).
618 Prediction Skill of the 2012 U.S. Great Plains Flash Drought in Subseasonal Experiment (SubX)
619 Models, *Journal of Climate*, 33(14), 6229-6253, <https://doi.org/10.1175/JCLI-D-19-0863.1>.

620 Ding, Q. and B. Wang. (2005). Circumglobal Teleconnection in the Northern Hemisphere
621 Summer. *J. Climate*, 18, 3483–3505, <https://doi.org/10.1175/JCLI3473.1>

622 Ding, Q., Wang, B., Wallace, J.M., and Branstator, G. (2011). Tropical–Extratropical
623 Teleconnections in Boreal Summer: Observed Interannual Variability. *J. Climate* 24: 1878–
624 1896. <https://doi.org/10.1175/2011JCLI3621.1>

625 Dirmeyer, P.A., M.J. Fennessy, and L. Marx. (2003). Low Skill in Dynamical Prediction of
626 Boreal Summer Climate: Grounds for Looking beyond Sea Surface Temperature. *J. Climate*, 16,
627 995–1002, [https://doi.org/10.1175/1520-0442\(2003\)016<0995:LSIDPO>2.0.CO;2](https://doi.org/10.1175/1520-0442(2003)016<0995:LSIDPO>2.0.CO;2).

628 Du, Y., Li, T., Xie, Z. et al. (2016). Interannual variability of the Asian subtropical westerly jet
629 in boreal summer and associated with circulation and SST anomalies. *Clim Dyn* 46: 2673.
630 <https://doi.org/10.1007/s00382-015-2723-x>.

631 Ha, K. J., Seo, Y. W., Lee, J. Y., Kripalani, R. H., & Yun, K. S. (2018). Linkages between the
632 South and East Asian summer monsoons: a review and revisit. *Climate dynamics*, 51(11), 4207-
633 4227, <https://doi.org/10.1007/s00382-017-3773-z>.

634 Hao, Z., Singh, V. P., & Xia, Y. (2018). Seasonal drought prediction: Advances, challenges,
635 and future prospects. *Reviews of Geophysics*, 56, 108–
636 141. <https://doi.org/10.1002/2016RG000549>

637 Henderson, S. A., Maloney, E. D., & Son, S. (2017). Madden–Julian Oscillation Pacific
638 Teleconnections: The Impact of the Basic State and MJO Representation in General Circulation
639 Models, *Journal of Climate*, 30(12), 4567-4587, <https://doi.org/10.1175/JCLI-D-16-0789.1>.

640 Hersbach, H., Bell, B., Berrisford, P., Hirahara, S., Horányi, A., Muñoz-Sabater, J., ...
641 & Thépaut, J. N. (2020). The ERA5 global reanalysis. *Quarterly Journal of the Royal*
642 *Meteorological Society*, 146(730), 1999-2049, <https://doi.org/10.1002/qj.3803>.

643 Hu, Q. and Feng, S. (2012). AMO- and ENSO-Driven Summertime Circulation and Precipitation
644 Variations in North America. *J. Climate* 25: 6477–6495, [https://doi.org/10.1175/JCLI-D-11-](https://doi.org/10.1175/JCLI-D-11-00520.1)
645 [00520.1](https://doi.org/10.1175/JCLI-D-11-00520.1).

646 Hu, Z. Z., Kumar, A., Jha, B., & Huang, B. (2020). How much of monthly mean precipitation
647 variability over global land is associated with SST anomalies?. *Climate Dynamics*, 54(1), 701-
648 712, <https://doi.org/10.1007/s00382-019-05023-5>.

649 Huang, B., Thorne, P.W., Banzon, V.F., Boyer, T., Chepurin, G., Lawrimore, J.H., Menne, M.J.,
650 Smith, T.M., Vose, R.S., & Zhang, H. (2017). Extended Reconstructed Sea Surface Temperature,
651 Version 5 (ERSSTv5): Upgrades, Validations, and Intercomparisons. *J. Climate* 30: 8179–8205,
652 <https://doi.org/10.1175/JCLI-D-16-0836.1>.

653 Jha, B., Kumar, A., & Hu, Z. Z. (2019). An update on the estimate of predictability of seasonal
654 mean atmospheric variability using North American Multi-Model Ensemble. *Climate Dynamics*,
655 53(12), 7397-7409. <https://doi.org/10.1007/s00382-016-3217-1>.

656 Jong, B., Ting, M., & Seager, R. (2021). Assessing ENSO Summer Teleconnections, Impacts,
657 and Predictability in North America, *Journal of Climate*, 34(9), 3629-3643,
658 <https://doi.org/10.1175/JCLI-D-20-0761.1>.

659 Kim, D., Lee, S., Lopez, H., & Goes, M. (2020). Pacific Mean-State Control of Atlantic
660 Multidecadal Oscillation–El Niño Relationship, *Journal of Climate*, 33(10), 4273-
661 4291, <https://doi.org/10.1175/JCLI-D-19-0398.1>.

662 Kirtman, B. P., D. A. Paolino, J. L. Kinter III and D. M. Straus. (2001). Impact of
663 tropical subseasonal SST variability on seasonal mean climate. *Mon. Wea. Rev.*, 129, 853-
664 868, [https://doi.org/10.1175/1520-0493\(2001\)129<0853:IOTSSV>2.0.CO;2](https://doi.org/10.1175/1520-0493(2001)129<0853:IOTSSV>2.0.CO;2).

665 Koster, R. D., Sud, Y. C., Guo, Z., Dirmeyer, P. A., Bonan, G., Oleson, K. W., ... & Xue, Y.
666 (2006). GLACE: the global land–atmosphere coupling experiment. Part I: overview. *Journal of*
667 *Hydrometeorology*, 7(4), 590-610, <https://doi.org/10.1175/JHM510.1>.

668 Lau, W., and H. Weng. (2002). Recurrent Teleconnection Patterns Linking Summertime
669 Precipitation Variability over East Asia and North America. *J Meteorol. Soc. Jpn*, 80, 1309-
670 1324., 10.2151/jmsj.80.1309, <https://doi.org/10.2151/jmsj.80.1309>.

671 Lee, J. Y., Wang, B., Ding, Q., Ha, K. J., Ahn, J. B., Kumar, A., ... & Alves, O. (2011). How
672 predictable is the Northern Hemisphere summer upper-tropospheric circulation?. *Climate*
673 *dynamics*, 37(5), 1189-1203, <https://doi.org/10.1007/s00382-010-0909-9>.

674 Lee, S., Wang, B. (2016). Regional boreal summer intraseasonal oscillation over Indian Ocean
675 and Western Pacific: comparison and predictability study. *Clim Dyn* 46, 2213–2229,
676 <https://doi.org/10.1007/s00382-015-2698-7>.

677 Lee, S., Wang, C., & Mapes, B. E. (2009). A Simple Atmospheric Model of the Local and
678 Teleconnection Responses to Tropical Heating Anomalies, *Journal of Climate*, 22(2), 272-284,
679 <https://doi.org/10.1175/2008JCLI2303.1>.

680 Li, J., Ding, R., Wu, Z., Zhong, Q., Li, B., & Li, J. (2019). Inter-decadal change in potential
681 predictability of the East Asian summer monsoon. *Theoretical and Applied Climatology*, 136(1),
682 403-415, <https://doi.org/10.1007/s00704-018-2482-9>.

683 Liu, A.Z., M. Ting, and H. Wang. (1998). Maintenance of Circulation Anomalies during the
684 1988 Drought and 1993 Floods over the United States. *J. Atmos. Sci.*, 55, 2810–2832,
685 [https://doi.org/10.1175/1520-0469\(1998\)055<2810:MOCADT>2.0.CO;2](https://doi.org/10.1175/1520-0469(1998)055<2810:MOCADT>2.0.CO;2).

686 Liu, F., Li, T., Wang, H., Deng, L., & Zhang, Y. (2016). Modulation of Boreal
687 Summer Intraseasonal Oscillations over the Western North Pacific by ENSO, *Journal of Climate*,
688 29(20), 7189-7201, <https://doi.org/10.1175/JCLI-D-15-0831.1>.

689 Liu, Y., Ke, Z., & Ding, Y. (2019). Predictability of East Asian summer monsoon in seasonal
690 climate forecast models. *International Journal of Climatology*, 39(15), 5688-5701,
691 <https://doi.org/10.1002/joc.6180>.

692 Lopez, H., Lee, S.-K., Dong, S., Goni, G., Kirtman, B., Atlas, R., & Kumar, A. (2019). East
693 Asian Monsoon as a modulator of U.S. Great Plains heatwaves. *Journal of Geophysical Research*
694 : Atmospheres, 124, 6342–6358. <https://doi.org/10.1029/2018JD030151>.

695 Mallakpour, I., Villarini, G. (2016). Investigating the relationship between the frequency of
696 flooding over the central United States and large-scale climate, *Advances in Water Resources* 92:
697 159-171, <https://doi.org/10.1016/j.advwatres.2016.04.008>.

698 Malloy, K. M., & Kirtman, B. P. (2020). Predictability of Midsummer Great Plains Low-Level
699 Jet and Associated Precipitation, *Weather and Forecasting*, 35(1), 215-235,
700 <https://doi.org/10.1175/WAF-D-19-0103.1>.

701 Mariotti, A., Baggett, C., Barnes, E. A., Becker, E., Butler, A., Collins, D. C., Dirmeyer, P. A.,
702 Ferranti, L., Johnson, N. C., Jones, J., Kirtman, B. P., Lang, A. L., Molod, A., Newman, M.,
703 Robertson, A. W., Schubert, S., Waliser, D. E., & Albers, J. (2020). Windows of Opportunity for
704 Skillful Forecasts Subseasonal to Seasonal and Beyond, *Bulletin of the American Meteorological*
705 *Society*, 101(5), E608-E625, 2021, <https://doi.org/10.1175/BAMS-D-18-0326.1>.

706 Moon, J. Y., Wang, B., Ha, K. J., & Lee, J. Y. (2013). Teleconnections associated with Northern
707 Hemisphere summer monsoon intraseasonal oscillation. *Climate dynamics*, 40(11-12), 2761-
708 2774, <https://doi.org/10.1007/s00382-012-1394-0>.

709 Neale RB et al. (2010). Description of the NCAR Community Atmosphere Model (CAM 5.0).
710 NCAR technical note NCAR/TN-486+STR, National Center for Atmospheric Research,
711 Boulder.

712 O'Reilly, C.H., Woollings, T., Zanna, L., and Weisheimer, A. (2018). The Impact of Tropical
713 Precipitation on Summertime Euro-Atlantic Circulation via a Circumglobal Wave Train. *J.*
714 *Climate* 31: 6481–6504. <https://doi.org/10.1175/JCLI-D-17-0451.1>.

715 Pegion, P. J., and A. Kumar. (2010). Multimodel Estimates of Atmospheric Response to Modes
716 of SST Variability and Implications for Droughts. *J. Climate*, 23, 4327–4341,
717 <https://doi.org/10.1175/2010JCLI3295.1>.

718 Slater, L. J., G. Villarini, and A. A. Bradley. (2016). Evaluation of the skill of North-American
719 Multi-Model Ensemble (NMME) global climate models in predicting average and extreme
720 precipitation and temperature over the continental USA. *Climate Dyn.*,
721 <https://doi.org/10.1007/s00382-016-3286-1>.

722 Schubert, S.D., M.J. Suarez, P.J. Pegion, M.A. Kistler, and A. Kumar. (2002). Predictability of
723 Zonal Means during Boreal Summer. *J. Climate*, 15, 420–434, [https://doi.org/10.1175/1520-](https://doi.org/10.1175/1520-0442(2002)015<0420:POZMDB>2.0.CO;2)
724 [0442\(2002\)015<0420:POZMDB>2.0.CO;2](https://doi.org/10.1175/1520-0442(2002)015<0420:POZMDB>2.0.CO;2).

725 Schubert, S. D., Suarez, M. J., Pegion, P. J., Koster, R. D., & Bacmeister, J. T. (2008). Potential
726 Predictability of Long-Term Drought and Pluvial Conditions in the U.S. Great Plains, *Journal of*
727 *Climate*, 21(4), 802-816, <https://doi.org/10.1175/2007JCLI1741.1>.

728 Schubert, S., H. Wang, and M. Suarez/ (2011). Warm Season Subseasonal Variability and
729 Climate Extremes in the Northern Hemisphere: The Role of Stationary Rossby Waves. *J.*
730 *Climate*, 24, 4773–4792, <https://doi.org/10.1175/JCLI-D-10-05035.1>.

731 Sheffield, J., S.J. Camargo, R. Fu, Q. Hu, X. Jiang, N. Johnson, K.B. Karnauskas, S.T. Kim, J.
732 Kinter, S. Kumar, B. Langenbrunner, E. Maloney, A. Mariotti, J.E. Meyerson, J.D. Neelin, S.
733 Nigam, Z. Pan, A. Ruiz-Barradas, R. Seager, Y.L. Serra, D. Sun, C. Wang, S. Xie, J. Yu, T.
734 Zhang, and M. Zhao. (2013). North American Climate in CMIP5 Experiments. Part II:
735 Evaluation of Historical Simulations of Intraseasonal to Decadal Variability. *J. Climate* 26:
736 9247–9290, <https://doi.org/10.1175/JCLI-D-12-00593.1>.

737 Song, F., & Zhou, T. (2015). The crucial role of internal variability in modulating the decadal
738 variation of the East Asian summer monsoon–ENSO relationship during the twentieth century.
739 *Journal of Climate*, 28(18), 7093-7107, <https://doi.org/10.1175/JCLI-D-14-00783.1>.

740 Sperber, K. R., Annamalai, H., Kang, I. S., Kitoh, A., Moise, A., Turner, A., ... & Zhou, T.
741 (2013). The Asian summer monsoon: an intercomparison of CMIP5 vs. CMIP3 simulations of
742 the late 20th century. *Climate dynamics*, 41(9-10), 2711-2744, [https://doi.org/10.1007/s00382-](https://doi.org/10.1007/s00382-012-1607-6)
743 [012-1607-6](https://doi.org/10.1007/s00382-012-1607-6).

744 Tian, D., Wood, E. F., & Yuan, X. (2017). CFSv2-based sub-seasonal precipitation and
745 temperature forecast skill over the contiguous United States. *Hydrology and Earth System*
746 *Sciences*, 21(3), 1477-1490, <https://doi.org/10.5194/hess-21-1477-2017>.

747 Ting, M. and Wang, H. (1997). Summertime U.S. Precipitation Variability and Its Relation to
748 Pacific Sea Surface Temperature. *J. Climate* 10: 1853–1873, [https://doi.org/10.1175/1520-](https://doi.org/10.1175/1520-0442(1997)010<1853:SUSPVA>2.0.CO;2)
749 [0442\(1997\)010<1853:SUSPVA>2.0.CO;2](https://doi.org/10.1175/1520-0442(1997)010<1853:SUSPVA>2.0.CO;2).

750 Trenberth, K. E., Branstator, G.W., Karoly, D., Kumar, A., Lau, N.C-. & Ropelewski C. (1998).
751 Progress during TOGA in understanding and modeling global teleconnections associated with
752 tropical sea surface temperatures, *J. Geophys. Res.* 103(C7): 14291–14324,
753 <https://doi.org/10.1029/97JC01444>.

754 Islam, S., & Tang, Y. (2017). Simulation of different types of ENSO impacts on South Asian
755 Monsoon in CCSM4. *Climate Dynamics*, 48(3-4), 893-911, [https://doi.org/10.1007/s00382-016-](https://doi.org/10.1007/s00382-016-3117-4)
756 [3117-4](https://doi.org/10.1007/s00382-016-3117-4).

757 Islam, S., Tang, Y., & Jackson, P. L. (2013). Asian monsoon simulations by Community Climate
758 Models CAM4 and CCSM4. *Climate dynamics*, 41(9-10), 2617-2642, 0.1007/s00382-013-1752-
759 6.

760 Wang, J., Kim, H., Kim, D., Henderson, S. A., Stan, C., & Maloney, E. D. (2020). MJO
761 Teleconnections over the PNA Region in Climate Models. Part II: Impacts of the MJO and Basic
762 State, *Journal of Climate*, 33(12), 5081-5101, <https://doi.org/10.1175/JCLI-D-19-0865.1>.

763 Wang, B., R. Wu, and K. Lau. (2001). Interannual Variability of the Asian Summer Monsoon:
764 Contrasts between the Indian and the Western North Pacific–East Asian Monsoons. *J. Climate*,
765 14, 4073–4090, [https://doi.org/10.1175/1520-0442\(2001\)014<4073:IVOTAS>2.0.CO;2](https://doi.org/10.1175/1520-0442(2001)014<4073:IVOTAS>2.0.CO;2).

766 Wang, B., Wu, Z., Li, J., Liu, J., Chang, C. P., Ding, Y., & Wu, G. (2008). How to measure the
767 strength of the East Asian summer monsoon. *Journal of Climate*, 21(17), 4449-
768 4463, <https://doi.org/10.1175/2008JCLI2183.1>.

769 Weaver, S.J., Schubert, S., & Wang, H. (2009). Warm Season Variations in the Low-Level
770 Circulation and Precipitation over the Central United States in Observations, AMIP Simulations,
771 and Idealized SST Experiments. *J. Climate* 22: 5401–5420,
772 <https://doi.org/10.1175/2009JCLI2984.1>.

773 Weaver, S.J., Baxter, S., and Harnos, K. (2016). Regional Changes in the Interannual Variability
774 of U.S. Warm Season Precipitation. *J. Climate* 29: 5157–5173, [https://doi.org/10.1175/JCLI-D-](https://doi.org/10.1175/JCLI-D-14-00803.1)
775 [14-00803.1](https://doi.org/10.1175/JCLI-D-14-00803.1).

776 Wu, B., Zhou, T., & Li, T. (2009). Contrast of Rainfall–SST Relationships in the Western North
777 Pacific between the ENSO-Developing and ENSO-Decaying Summers, *Journal of Climate*,
778 22(16), 4398-4405, <https://doi.org/10.1175/2009JCLI2648.1>.

779 Xie, P., & Arkin, P. A. (1997). Global precipitation: A 17-year monthly analysis based on gauge
780 observations, satellite estimates, and numerical model outputs. *Bulletin of*
781 *the American Meteorological Society*, 78(11), 2539-2558, [https://doi.org/10.1175/1520-0477\(1997\)078<2539:GPAYMA>2.0.CO;2](https://doi.org/10.1175/1520-0477(1997)078<2539:GPAYMA>2.0.CO;2).

783 Yang, Y., Zhu, Z., Li, T., & Yao, M. (2020). Effects of western Pacific intraseasonal convection
784 on surface air temperature anomalies over North America. *International Journal of Climatology*,
785 40(6), 2913-2923, <https://doi.org/10.1002/joc.6373>.

786 Zhao, G., Huang, G., Wu, R., Tao, W., Gong, H., Qu, X., & Hu, K. (2015). A New Upper-Level
787 Circulation Index for the East Asian Summer Monsoon Variability, *Journal of Climate*, 28(24),
788 9977-9996, <https://doi.org/10.1175/JCLI-D-15-0272.1>.

789 Zhao, S., Y. Deng, and R.X. Black. (2018). An Intraseasonal Mode of Atmospheric Variability
790 Relevant to the U.S. Hydroclimate in Boreal Summer: Dynamic Origin and East Asia
791 Connection. *J. Climate*, 31, 9855–9868, <https://doi.org/10.1175/JCLI-D-18-0206.1>.

792 Zhou, F., Ren, H. L., Hu, Z. Z., Liu, M. H., Wu, J., & Liu, C. Z. (2020). Seasonal predictability
793 of primary East Asian summer circulation patterns by three operational climate prediction
794 models. *Quarterly Journal of the Royal Meteorological Society*, 146(727), 629-646,
795 <https://doi.org/10.1002/qj.3697>.

796 Zhou, S., L'Heureux, M., Weaver, S. et al. (2012). A composite study of the MJO influence on
797 the surface air temperature and precipitation over the Continental United States. *Clim Dyn* 38,
798 1459–1471, <https://doi.org/10.1007/s00382-011-1001-9>.

799 Zhu, J., Huang, B., Hu, Z. Z., Kinter, J. L., & Marx, L. (2013). Predicting US summer
800 precipitation using NCEP Climate Forecast System version 2 initialized by multiple ocean
801 analyses. *Climate dynamics*, 41(7-8), 1941-1954, <https://doi.org/10.1007/s00382-013-1785-x>.

802 Zhu, Z. and T. Li. (2016). A New Paradigm for Continental U.S. Summer Rainfall Variability:
803 Asia–North America Teleconnection. *J. Climate*, 29, 7313–7327, [https://doi.org/10.1175/JCLI-](https://doi.org/10.1175/JCLI-D-16-0137.1)
804 [D-16-0137.1](https://doi.org/10.1175/JCLI-D-16-0137.1).

805 Zhu, Z. and T. Li. (2018). Amplified contiguous United States summer rainfall variability
806 induced by East Asian monsoon interdecadal change. *Clim Dyn* 50: 3523.
807 <https://doi.org/10.1007/s00382-017-3821-8>.

808

809

Figures

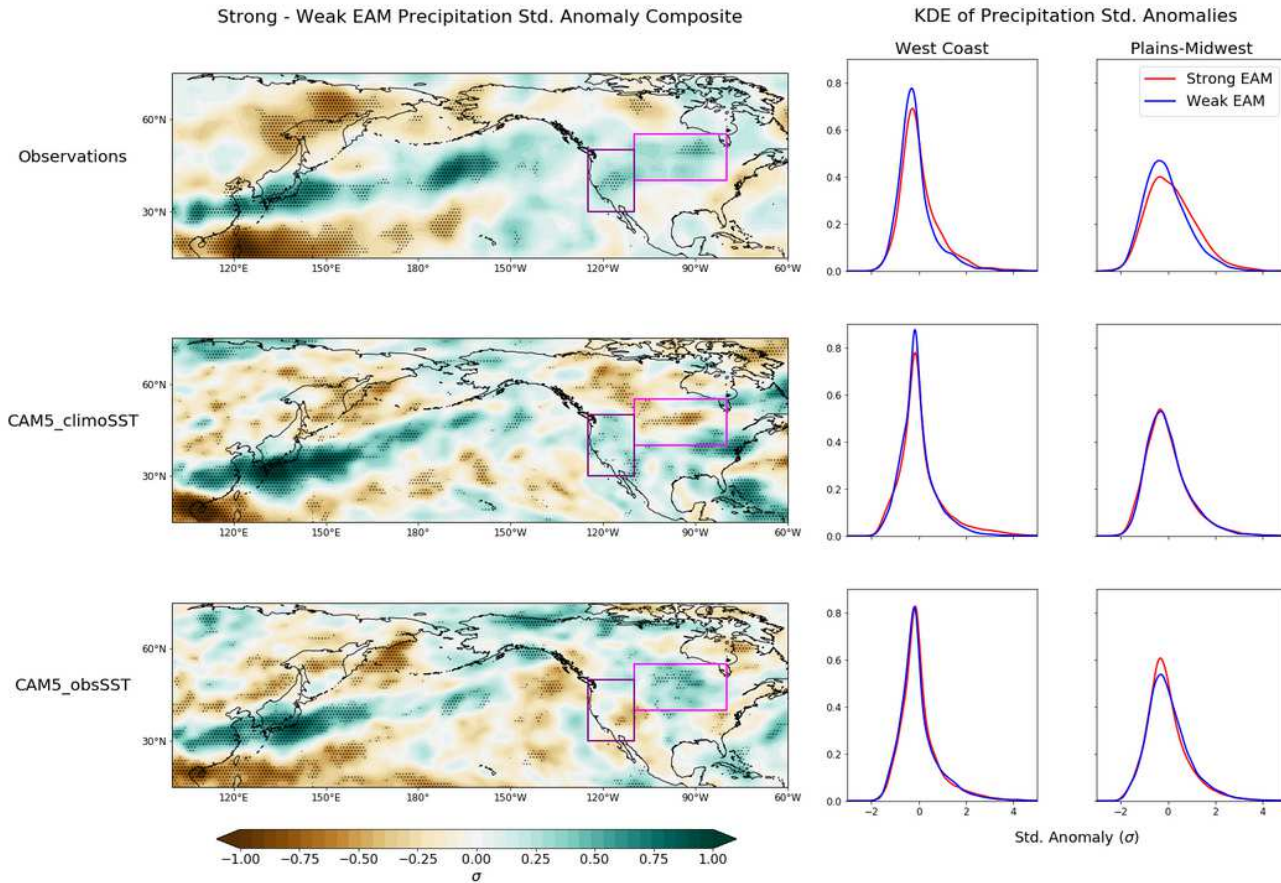


Figure 1

(left column) Strong – weak EAM precipitation standardized anomaly composites for (top) CMAP observations, (middle) CAM5_climoSST, the CAM5 experiment with prescribed climatological SSTs, and (bottom) CAM5_obsSST, the CAM5 experiment with prescribed observed SSTs. Stippling indicates anomalies significant at the 90% confidence level. Purple and magenta boxes denote West Coast and Plains-Midwest domains, respectively. (middle and right columns) Kernel density estimators of the precipitation standardized anomalies for the grid points corresponding to the (middle) West Coast and (right) Plains-Midwest domains for (red solid) strong EAM months and (blue solid) weak EAM months.

Strong - Weak EAM Z250' *

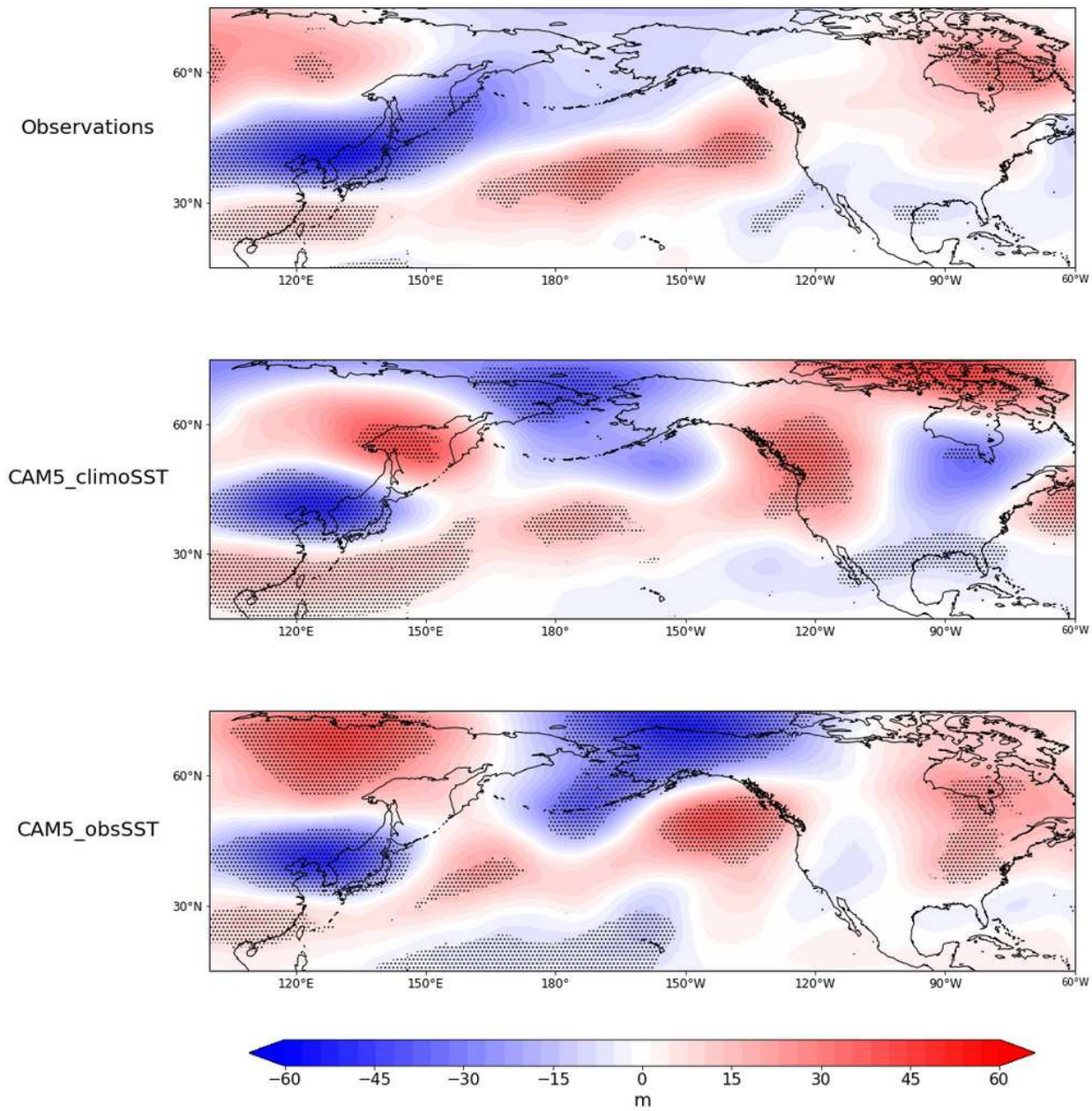


Figure 2

Zonally-asymmetric component of strong – weak EAM Z250 anomaly composites for (top) ERA5 observations, (middle) CAM5_climoSST experiment, and (bottom) CAM5_obsSST experiment.

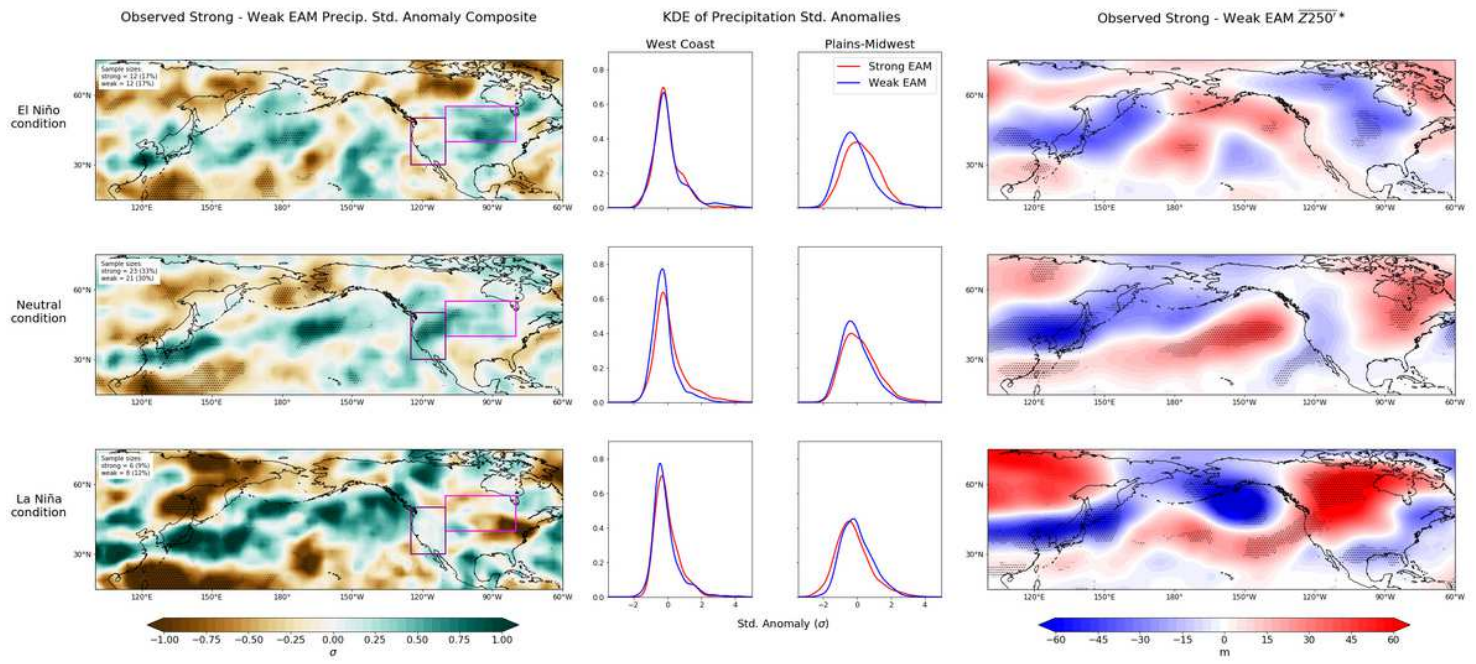


Figure 3

(left column) Observed strong – weak EAM precipitation standardized anomaly composites during (top) El Niño conditions, (middle) neutral ENSO conditions, and (bottom) La Niña conditions. Purple and magenta boxes denote West Coast and Plains-Midwest domains, respectively. Stippling indicates anomalies significant at the 90% confidence level. Sample sizes for composites are also annotated in upper-left corner. (middle columns) Kernel density estimators of the precipitation standardized anomalies for the grid points corresponding to the (middle-left) West Coast and (middle-right) Plains-Midwest domains for (red) strong EAM months and (blue) weak EAM months. (right column) Observed zonally-asymmetric component of strong – weak EAM Z250 composites during (top) El Niño conditions, (middle) neutral ENSO conditions, and (bottom) La Niña conditions.

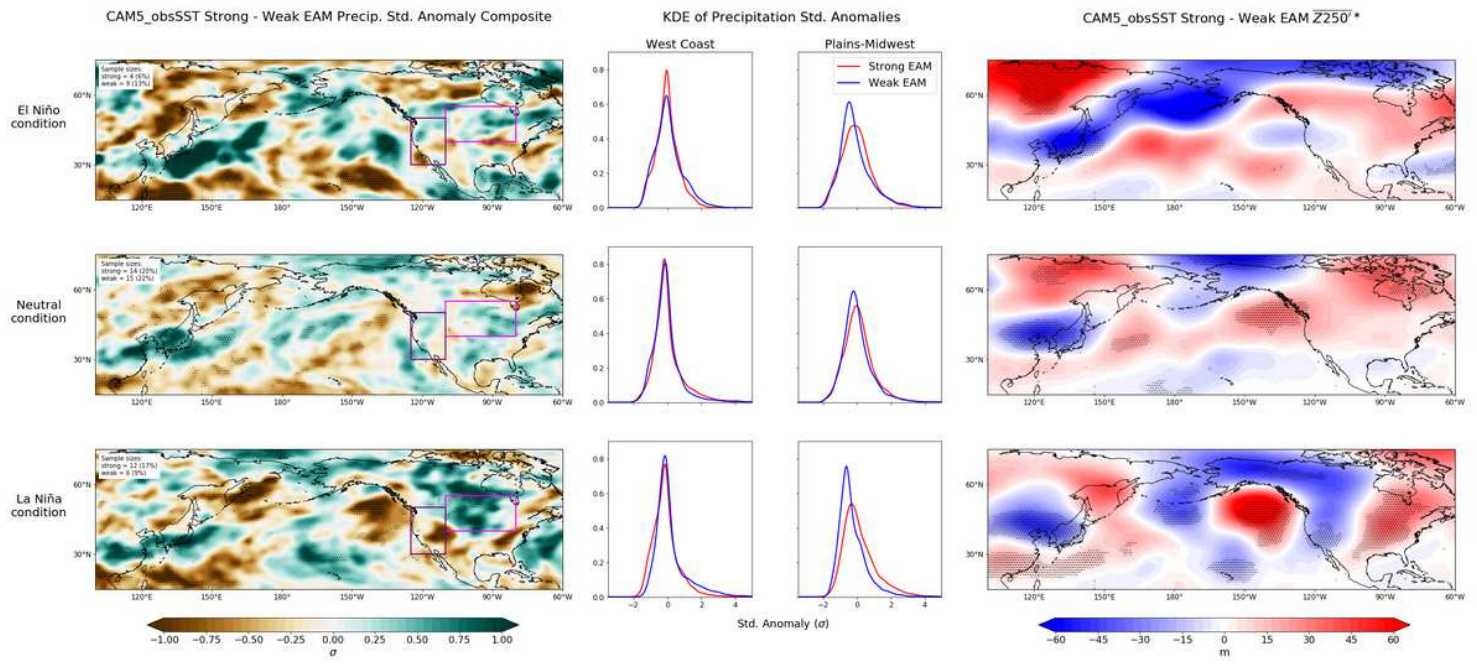


Figure 4

Same as Fig. 3, but for CAM5_obsSST experiment.

Steady-state linear QG solutions of EAM-forced Z250 anomalies

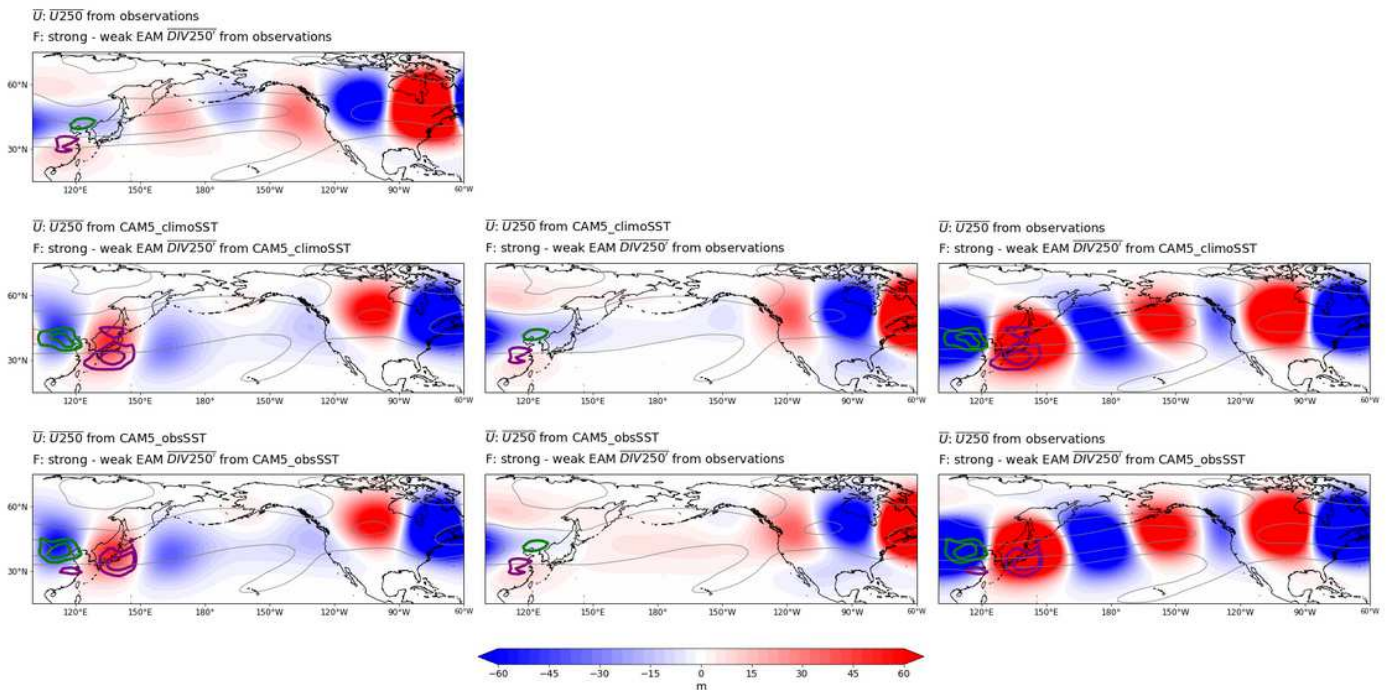


Figure 5

Linear steady-state QG solutions of Z250 with \bar{U} and F from (left column) (top) observations, (middle) CAM5_climoSST experiment, and (bottom) CAM5_obsSST experiment. (middle column) Solutions of

Z250 with \bar{U} from observations and \bar{U} from (top) CAM5_climoSST experiment and (bottom) CAM5_obsSST experiment. (right column) Solutions of Z250 with \bar{U} from observations and F from (top) CAM5_climoSST experiment and (bottom) CAM5_obsSST experiment. The corresponding \bar{U} is overlaid in light gray with contours of 10 and 20 m s⁻¹. The corresponding F is overlaid, with thick green contours as -0.5 and -1 s⁻¹ x10⁻⁶ and thick purple contours as 0.5 and 1 s⁻¹ x10⁻⁶.

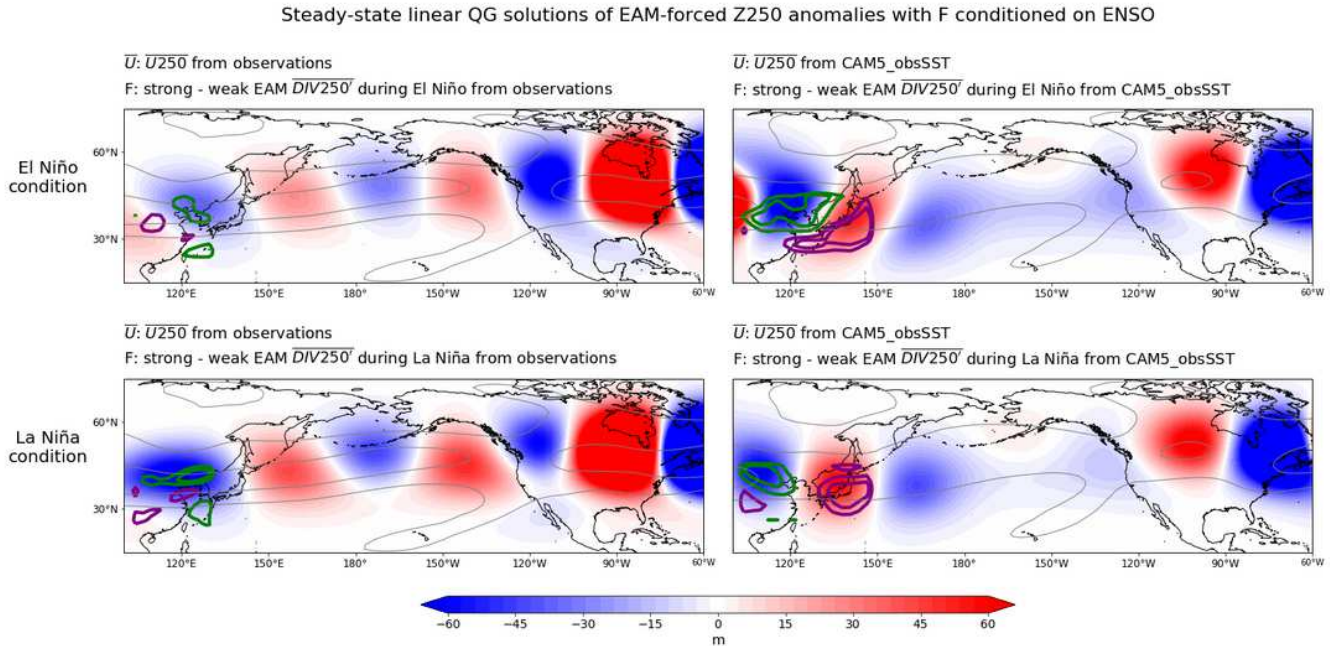


Figure 6

Linear steady-state QG solutions of Z250 with \bar{U} and F from (left column) observations and (right column) CAM5_climoSST experiment. (top row) Solutions when F is conditioned on El Niño, and (bottom row) solutions when F is conditioned on La Niña. The corresponding \bar{U} is overlaid in light gray with contours of 10 and 20 m s⁻¹. The corresponding F is overlaid, with thick green contours as -0.5 and -1 s⁻¹ x10⁻⁶ and thick purple contours as 0.5 and 1 s⁻¹ x10⁻⁶.

Steady-state linear QG solutions of EAM-forced Z250 anomalies with \bar{U} conditioned on ENSO

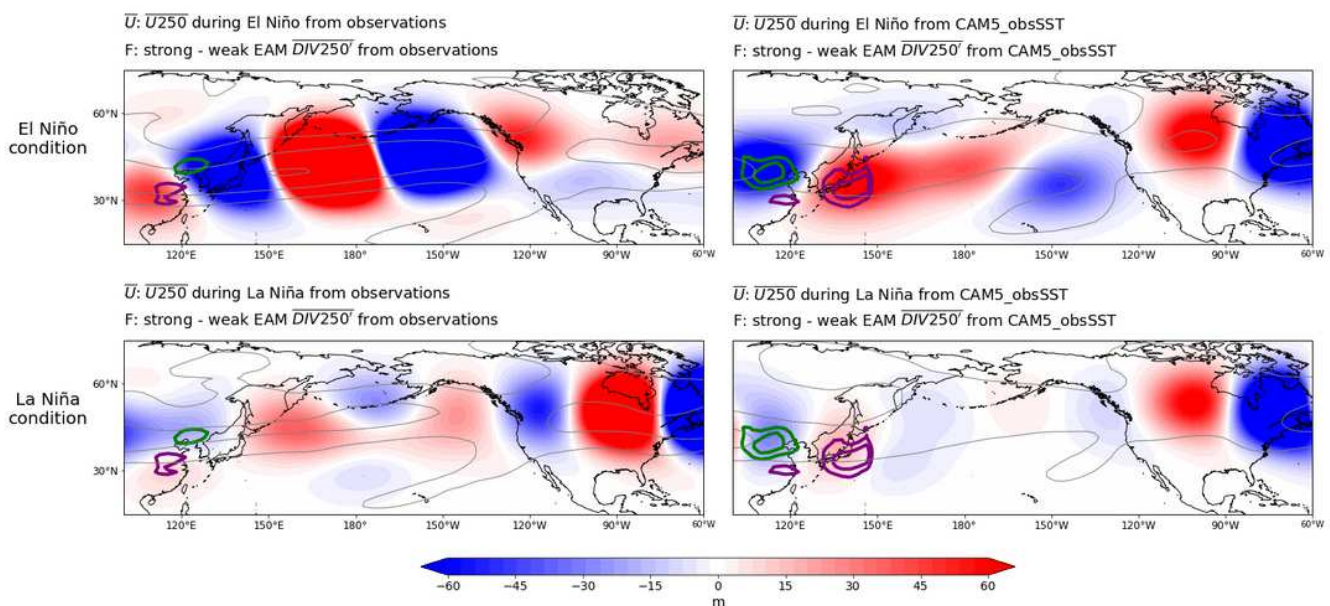


Figure 7

Same as Fig. 6, but when \bar{U} is conditioned on (top row) El Niño and (bottom row) La Niña.

ENSO-modulated part of linear QG solutions of Z250 anomalies

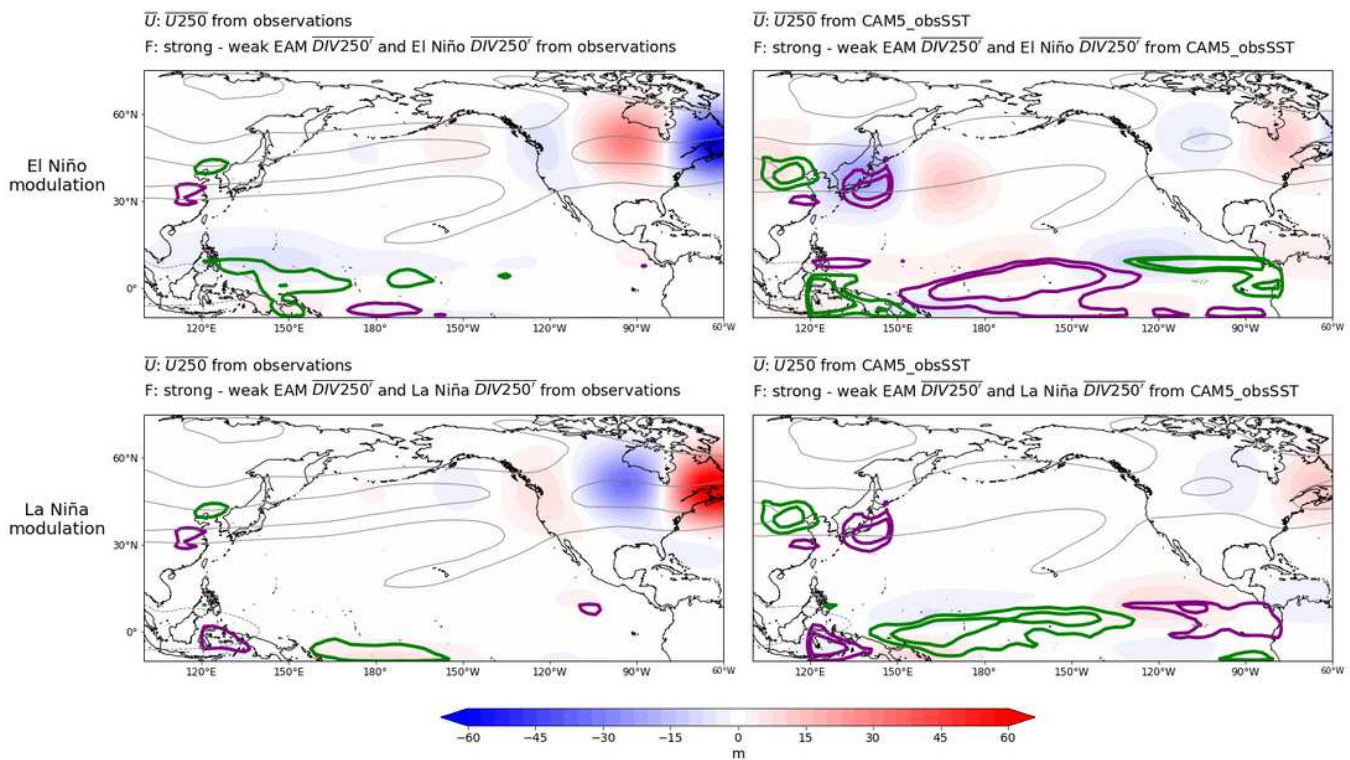


Figure 8

ENSO-modulated part of the steady-state linear QG solutions with \bar{U} and F from (left column) observations and (right column) CAM5_climoSST experiment. (top row) Solutions when F includes El Niño-related divergence anomalies, and (bottom row) solutions when F includes La Niña-related divergence anomalies. The corresponding \bar{U} is overlaid in light gray with contours of 10 and 20 m s⁻¹. The corresponding F is overlaid, with thick green contours as -0.5 and -1 s⁻¹ x10⁻⁶ and thick purple contours as 0.5 and 1 s⁻¹ x10⁻⁶.

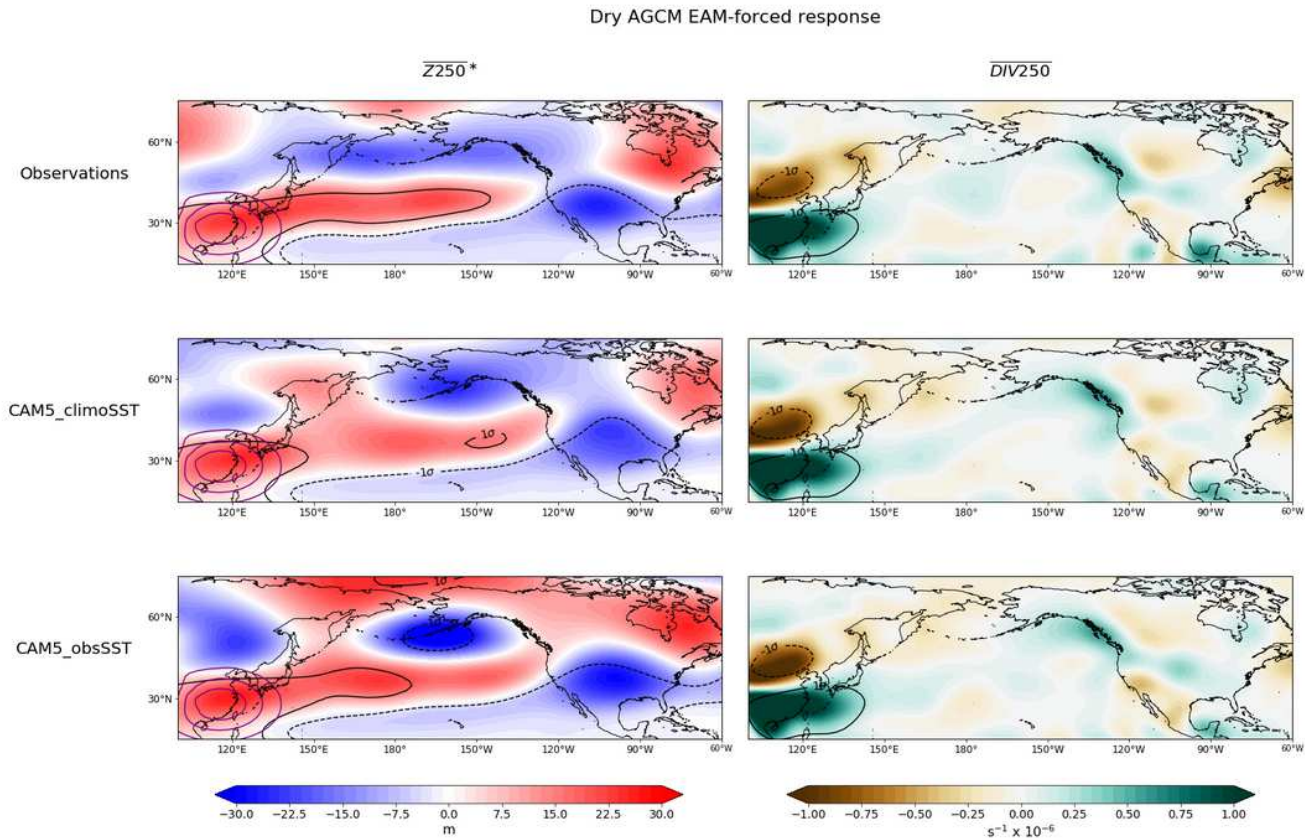


Figure 9

Dry AGCM EAM heating response, including the (left column) asymmetric component of the time-mean Z250 and (right column) time-mean DIV250, for when the inputted mean state is from (top row) observations, (middle row) CAM5_climoSST experiment, and (bottom row) CAM5_obsSST experiment. The 1σ (solid black) and -1σ (dashed black) values – calculated by dividing response by divided by the 90-day moving mean σ – are overlaid, representing $\sim 67\%$ of the variability of the response assuming Gaussian statistics. Heating forcing (purple contours) of 0.5, 1, and 1.5 K day⁻¹ are also overlaid on Z250 responses.

Difference in EAM-forced response when mean state conditioned on El Niño

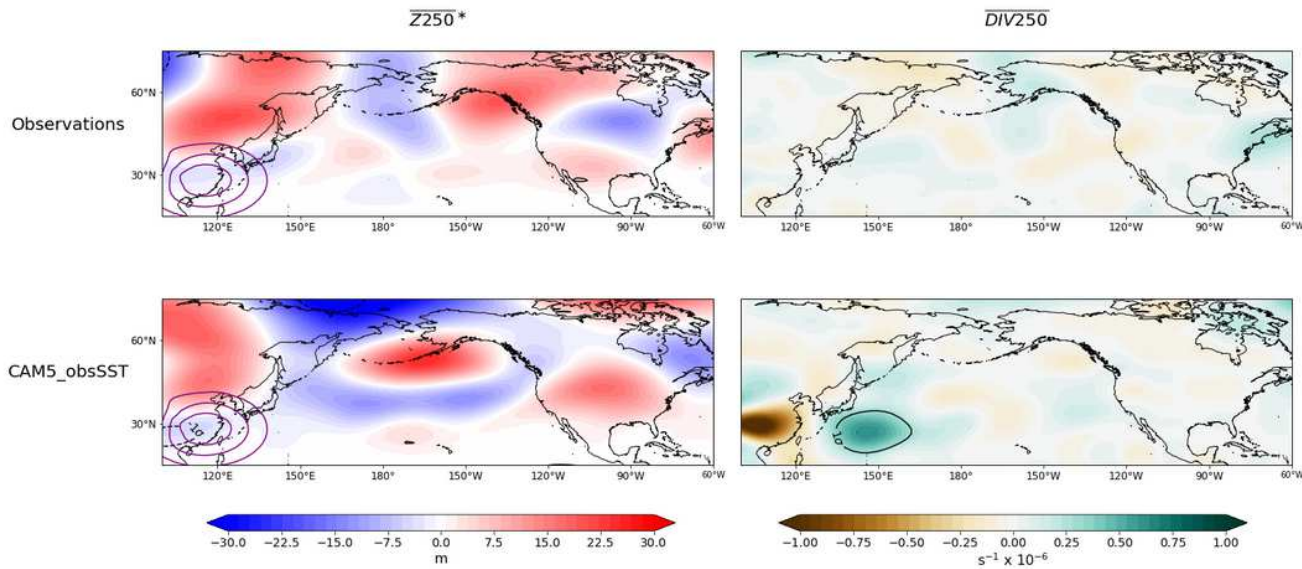


Figure 10

Difference in dry AGCM EAM heating response from Fig. 9, including the (left column) asymmetric component of the time-mean Z250 and (right column) time-mean DIV250, for when the inputted mean state is taken during El Niño from (top row) observations and (bottom row) CAM5_obsSST experiment. The 1σ (solid black) and -1σ (dashed black) values are overlaid. Heating forcing (purple contours) are the same as Fig. 9.

Difference in EAM-forced response when mean state conditioned on La Niña

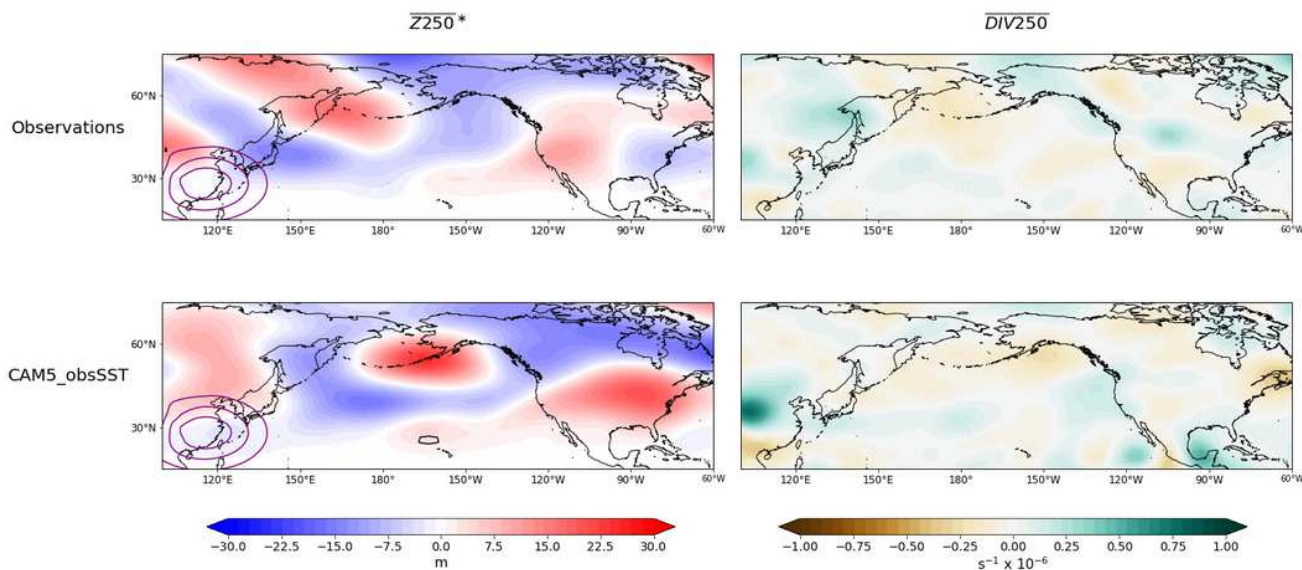


Figure 11

Same as Fig. 10, but for mean state taken during La Niña.

Dry AGCM El Niño-modulated part of response

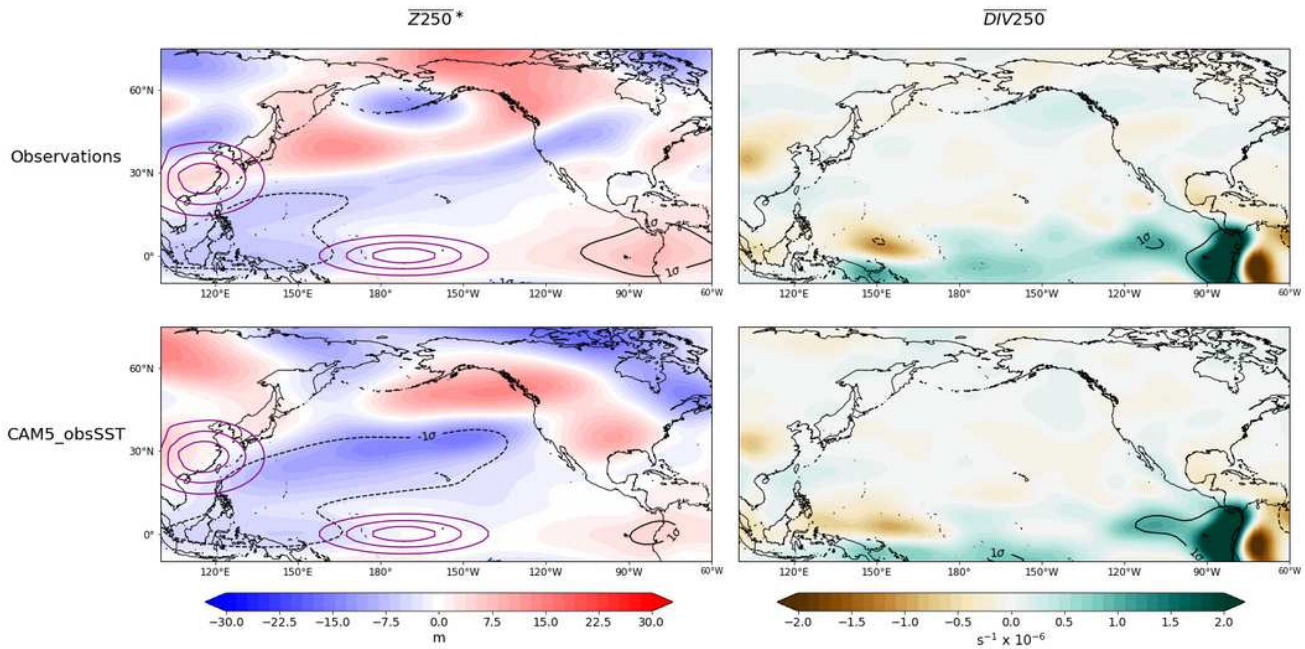


Figure 12

Dry AGCM El Niño-modulated part of the heating response (see Table 1 for details). (left column) asymmetric component of the time-mean Z250 and (right column) time-mean DIV250, for when the inputted mean state is taken from (top row) observations and (bottom row) CAM5_obsSST experiment. The 1 σ (solid black) and -1 σ (dashed black) values are overlaid. Heating forcing (purple contours) of 0.5, 1, and 1.5 K day⁻¹ from combined EAM- and El Niño-forced experiment are also overlaid on Z250 responses.

Dry AGCM La Niña-modulated part of response

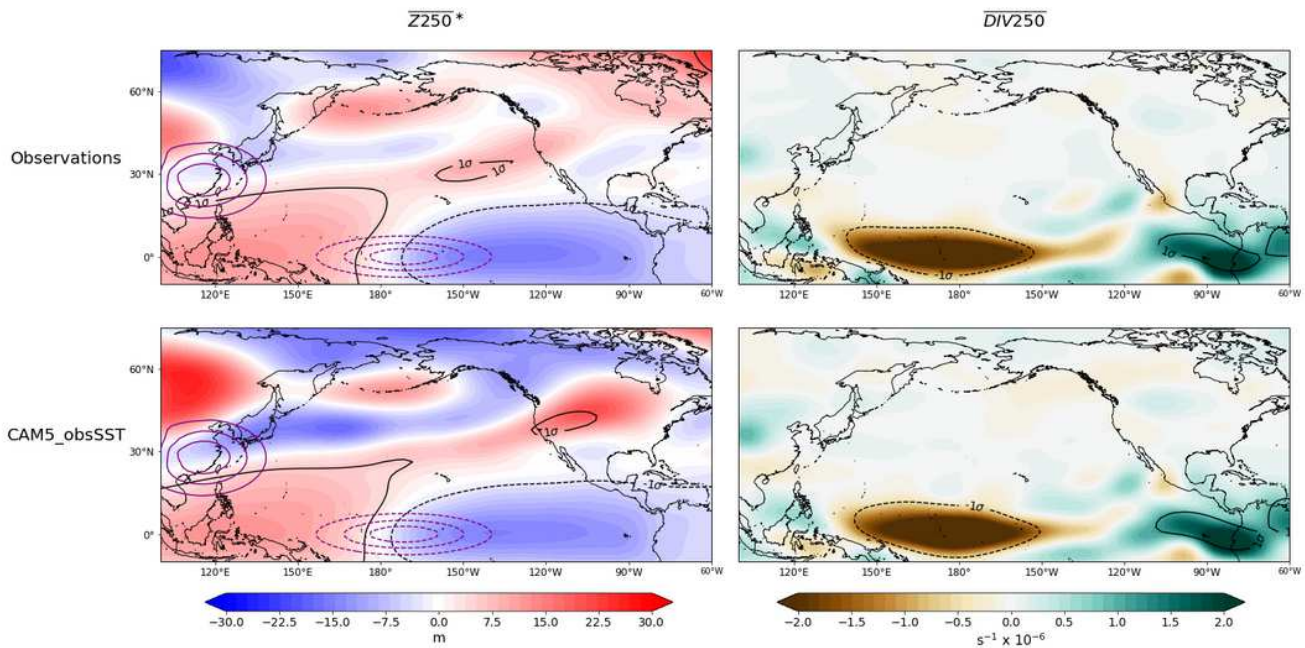


Figure 13

Same as Fig. 12, but the La Niña-modulated part of the heating response. Heating forcing (purple contours) of -0.5, -1, and -1.5 K day⁻¹ are included.